AFRL-AFOSR-VA-TR-2022-0102

Understanding ultrafast and nanoscale electron emission and transport

Peng Zhang
MICHIGAN STATE UNIVERSITY
426 AUDITORIUM RD RM 2
EAST LANSING, MI, 48824
USA

02/13/2022
Final Technical Report

Air Force Research Laboratory
Air Force Office of Scientific Research
Arlington, Virginia 22203
Air Force Materiel Command

REPORT DOCUMENTATION PAGE

PLEASE DO NOT RETURN YOUR FORM TO THE ABOVE ORGANIZATION.

1. REPORT DATE	2. REPORT TYPE	3. DATES COVERED	
20220213	Final	START DATE 20171201	END DATE 20211130

4. TITLE AND SUBTITLE
Understanding ultrafast and nanoscale electron emission and transport

5a. CONTRACT NUMBER	5b. GRANT NUMBER	5c. PROGRAM ELEMENT NUMBER
	FA9550-18-1-0061	61102F
5d. PROJECT NUMBER	**5e. TASK NUMBER**	**5f. WORK UNIT NUMBER**

6. AUTHOR(S)
Peng Zhang

7. PERFORMING ORGANIZATION NAME(S) AND ADDRESS(ES)
MICHIGAN STATE UNIVERSITY
426 AUDITORIUM RD RM 2
EAST LANSING, MI 48824
USA

8. PERFORMING ORGANIZATION REPORT NUMBER

9. SPONSORING/MONITORING AGENCY NAME(S) AND ADDRESS(ES)	10. SPONSOR/MONITOR'S ACRONYM(S)	11. SPONSOR/MONITOR'S REPORT NUMBER(S)
Air Force Office of Scientific Research 875 N. Randolph St. Room 3112 Arlington, VA 22203	AFRL/AFOSR RTB1	AFRL-AFOSR-VA-TR-2022-0102

12. DISTRIBUTION/AVAILABILITY STATEMENT
A Distribution Unlimited: PB Public Release

13. SUPPLEMENTARY NOTES

14. ABSTRACT
This AFOSR YIP award has substantially enhanced the PI's career development and built a solid foundation for the PI's future research. The research contributed to theoretical advances in: (A) Physics of diodes and ultrafast electron emission, (B) Electrical contacts and heating phenomenology, (C) Electron beam-circuit interaction, (D) Relativistic plasma physics in supercritical fields, and (E) Gas breakdown and plasma discharge. In area (A), we develop exact, analytical quantum theory for photoemission from solid surfaces and nanogaps. The exact theory considers various practical configurations, including DC bias, single frequency laser, two-color laser, two lasers of the same frequency, few-cycle laser pulses, and laser pulse train. We explore to enhance photo- and field- emission using ultrathin dielectric coatings. We analyze quantum efficiency for lasers from ultraviolet to near-infrared. We develop a generalized self-consistent model for quantum tunneling, covering Simmons law, FowlerNordheim law, the classical and quantum Child-Langmuir law in various limits, with their transition and current rectification. In collaboration with AFRL, we study field emission from carbon nanotube (CNT) fiber cathodes and secondary electron emission reduction of laser drilled micro-porous surfaces. We also publish a major, invited Perspective article, entitled, "Space-charge limited current in nanodiodes: Ballistic, collisional, and dynamical effects". In area (B), we develop a self-consistent two-dimensional (2D) transmission line model to investigate current crowding and intense heating profiles at contacts and junctions with varying geometries and resistivities along the contact interface. It is successfully applied to ohmic, tunneling, and 2D-material-based Schottky contacts.

15. SUBJECT TERMS

16. SECURITY CLASSIFICATION OF:			17. LIMITATION OF ABSTRACT	18. NUMBER OF PAGES
a. REPORT	b. ABSTRACT	c. THIS PAGE		
U	U	U	UU	43

19a. NAME OF RESPONSIBLE PERSON	19b. PHONE NUMBER *(Include area code)*
JULIE MOSES	426-9586

Final Technical Report

Understanding ultrafast and nanoscale electron emission and transport

AFOSR YIP Grant Number: FA9550-18-1-0061

Performance Period: 12/01/2017 – 11/30/2021

Submitted to:

Dr. John Luginsland and Dr. Ali Sayir

Air Force Office of Scientific Research

john.luginsland@us.af.mil

ali.sayir.2@us.af.mil

Submitted by:

Associate Professor Peng Zhang (PI)

Michigan State University, East Lansing, MI 48824-1226

pz@egr.msu.edu, Tel: (517) 353-3654

January 6, 2022

Table of Contents

1.0 Executive Summary

This Air Force Office of Scientific Research (AFOSR) Young Investigator Research Program (YIP) award has substantially enhanced the PI's career development as a university professor since joining Michigan State University in 2016 and helped the PI build a solid foundation for his future research directions. A variety of research topics on ultrafast and nanoscale electron emission and transport were studied, which include: (A) Physics of diodes and ultrafast electron emission, (B) Electrical contacts and heating phenomenology, (C) Electron beam-circuit interaction, (D) Relativistic plasma physics in supercritical fields, and (E) Gas breakdown and plasma discharge. The accomplishments on each are given below.

A. Physics of diodes and ultrafast electron emission

1. We develop exact, analytical quantum theory for the highly nonlinear ultrafast photoemission from solid surfaces and nanogaps that are subjected to an arbitrary combination of DC bias and laser fields. The exact theory considers photoemission with various practical configurations, including single frequency laser, two-color laser, two lasers of the same frequency, few-cycle laser pulses, and laser pulse train, all of which are analytically solved for the first time.

2. We demonstrate a practical way to enhance photoemission current with low intensity lasers, by using plasmonic resonance due to ultrathin dielectric coatings. A US patent is filed.

3. We systematically analyze quantum efficiency of photoemission with lasers from ultraviolet to near-infrared, for the first time. Our model reproduces previous experimental results.

4. We study field emission from a single carbon nanotube (CNT) fiber and CNT fiber array cathodes developed at AFRL. Effects of contact resistance and array dimensions are highlighted.

5. We develop a self-consistent model for quantum tunneling current in dissimilar metal-insulator-metal junctions. This is the most general scaling law for tunneling current to date. It covers the Simmons law, Fowler-Nordheim law, the classical and quantum Child-Langmuir law in various limits, including their transition and current rectification.

6. In collaboration with AFRL, we study secondary electron emission reduction of laser drilled micro-porous gold surfaces using empirical modeling and Monte Carlo simulation.

7. We present an exact analytical theory for field emission from dielectric coated cathode surfaces, showing significant enhancement of emission current with coating. Our study provides insights for designing field emitters with higher efficiency and better stability.

8. We publish a major, invited Perspective article, entitled, "Space-charge limited current in nanodiodes: Ballistic, collisional, and dynamical effects".

9. We provide direct imaging of high-temperature electron plasma waves using ultrafast electron microscopy, demonstrating unprecedented high spatiotemporal resolutions.

B. Electrical contacts and heating phenomenology

10. We develop a self-consistent two-dimensional (2D) transmission line model to investigate current crowding and intense heating profiles at contacts and junctions with varying geometries and resistivities along the contact interface. The model covers regimes inaccessible to existing finite element and transmission line methods commonly used for semiconductor characterization. It is successfully applied to ohmic, tunneling, and 2D-material-based Schottky contacts.

11. We propose to reduce contact resistance in 2D material-based electrical contacts by roughness engineering, offering a possible paradigm to solve one of the major challenges in 2D-material-based electronics and optoelectronics. Contacts of irregular geometry are also analyzed.

12. We demonstrate contact interface engineering to mitigate current crowding near electrical contacts by spatially designing the interface layer thickness or properties, without requiring an additional material or component. Because of the novelty, our method is awarded a US Patent.

13. We compare the temperature distribution of a looped CNT fiber emitter with a traditional single vertical CNT fiber emitter. A recent theory on joule heating of a one-dimensional conductor is successfully applied to explain the AFRL experimental measurements.

C. Electron beam-circuit interaction

14. We write an invited Review article on beam-circuit interactions for traveling wave tubes.

15. We apply a discrete cavity model to study coupled cavity travelling wave tubes. It allows us to treat individually tunable cavities, which is not possible with classical Pierce's theory.

16. We show Smith-Purcell (SP) radiation depends strongly on the grating parameters, which is rarely studied in the literature. We also explore to use SP to measure electron bunch properties.

D. Relativistic plasma physics in supercritical fields

17. We write an invited Perspective article on relativistic plasma physics in supercritical fields. The new plasma regime, where the physics of relativistic plasmas is strongly affected by strong-field quantum electrodynamics processes, is both of fundamental interest and crucial to applications such as high energy ion, electron, positron, and photon sources, medical radiotherapy, and next generation radiography for homeland security and industry.

E. Gas breakdown and plasma discharge

18. We study gas breakdown and plasma discharge in microgaps with a protrusive electrode. This results in a flattened Paschen's curve, with relatively low breakdown voltages in a wider pressure range. A US provisional patent is filed for this novel method to control gas breakdown.

19. We study gas breakdown in microgaps with multiple concentric cathode protrusions, electron kinetics in microhollow cathode discharges, and plasma formation around microstructure arrays.

20. We study gas breakdown from macro to micro/nano scale gaps, similarity and frequency scaling of plasmas with varying ionization degrees, and effects of high-energy ballistic electrons.

2.0 Research Objectives

This proposal investigates several unsolved problems in electron emission and transport at ultrashort spatiotemporal scales.

The objective is to provide a foundational understanding of the underlying physics in ultrafast and nanoscale electron emission and transport. The goal is to provide a guideline for the design of advanced electron sources and nanoelectronic devices. We construct novel analytic theory for laser induced electron emission, allowing for arbitrary laser frequency, pulse profile, laser power, electrostatic bias, and multi-frequency laser illumination. Also examined are the laser electric field enhancement and the cathode performance under ultrafast condition. We explore electron emission from novel low dimensional materials. These analytical studies lead to useful scaling laws, which could explain, and propose, experiments on laser induced photoemission, in particular those being performed at Air Force Research Laboratory.

We develop theoretical models for ultrafast and nanoscale electron transport across interfaces. We investigate ultrafast tunneling current in a nanogap and space-charge-limited electron transport under oscillating bias. We explore current rectification in miniaturized diodes based on geometric asymmetry, and novel ways of controlling emission current uniformity and current crowding by a judicious design of electrical contact making use of tailored tunneling resistance. These theoretical endeavors represent a unique contribution to ultrafast nanoelectronics.

Electron dynamics and transport in beam-circuit interaction, relativistic plasmas, and gas breakdown and plasma discharges are also investigated.

3.0 Research Topics and Accomplishments

3.1 Physics of diodes and ultrafast electron emission

3.1.1 Exact analytical quantum theory for ultrafast photoemission

a. Two-color laser induced electron emission

Electron emission from solids driven by two-color lasers provides great flexibility for the control of electron dynamics in ultrashort spatiotemporal scales due to the interference effect. We constructed an analytical model for the highly nonlinear photoelectron emission from a metal surface illuminated by two-color laser fields, by solving the time-dependent Schrödinger equation [1]. The exact solution is valid for arbitrary harmonic orders, laser intensities, phase difference between two lasers, and metal work function and Fermi level. Various emission mechanisms, such as multiphoton absorption or emission, optical or dc field emission, are all included in this single formulation. We find two-color lasers can strongly modulate both the electron energy spectra and the emission current up to 99% (Fig. 1). Using the same input parameters, our theoretical prediction for the photoemission current modulation depth (93.9%) is almost identical to previous experimental result (94%) [1]. The results provide insights into the

electron pulse generation and manipulation for many novel applications based on ultrafast laser-induced electron emission.

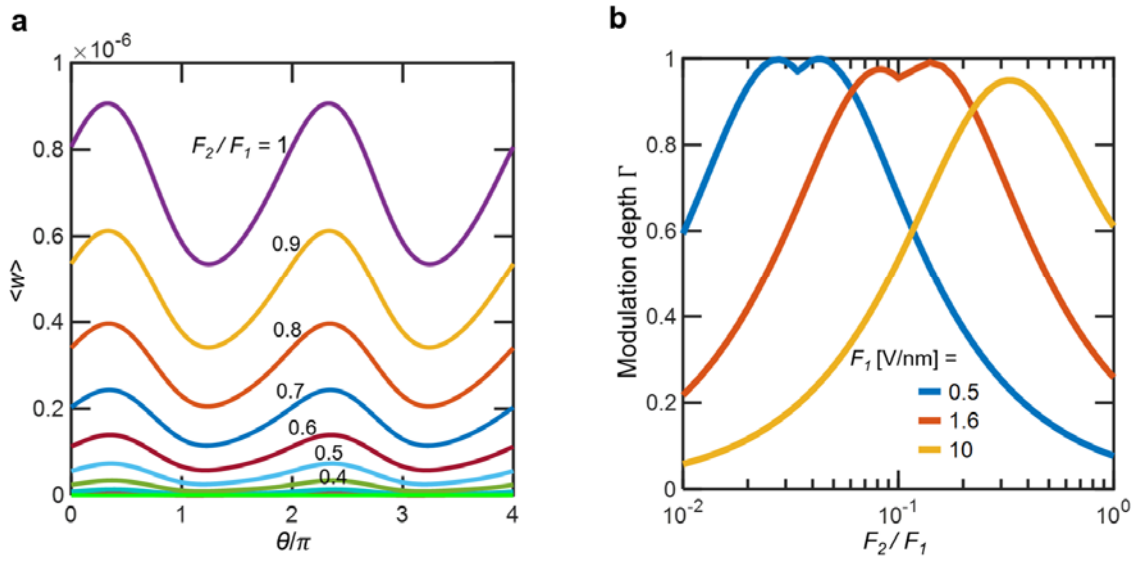

Fig. 1. (a) Time-averaged emission current density <*w*> due to two-color laser fields: the fundamental laser field $F_1\cos(\omega t)$ and harmonic laser field $F_2\cos(2\omega t+\theta)$, (b) current modulation depth $\Gamma = (\langle w\rangle_{max} - \langle w\rangle_{min})/(\langle w\rangle_{max} + \langle w\rangle_{min})$ for the different field ratios F_2/F_1. F_1 is fixed at 1.6 V/nm in a. Excerpt from [1].

b. Two-color laser induced electron emission from biased metal surfaces

In practice, besides the driven lasers, photoelectron emission from solids requires a DC bias to extract the emitted current. The effect of DC bias in photoemission is not well studied. By solving the time-dependent Schrödinger equation, we constructed an exact analytical solution for the nonlinear ultrafast electron emission from a dc biased metal surface illuminated by two-color laser fields [2]. We systematically examined the combined effects of a dc electric field and two-color laser fields. In addition to the remarkable tunability of electron emission processes due to interference from two-color laser fields, we find that a strong dc electric field not only opens up more tunneling emission channels, but also introduces intense modulation to the emission current. We find the surprising results that strong current modulation (with respect to the phase difference of the two-color lasers) persists (>70%), even with a large dc bias (i.e., ratio of the electric fields for dc : fundamental laser : second-harmonic laser ~= 1 : 0.5 : 0.07). In the meantime, the average emission current level increases by about three orders of magnitude relative to the case of zero dc bias. Application of our model to time-resolved photoelectron spectroscopy is exemplified and shows that the dynamics of the *n*-photon excited states depends strongly on the applied dc field (Fig. 2). Our study suggests a practical way to maintain a strong modulation to high current photoemission, by the addition of a large dc bias for two-color laser-induced electron emission.

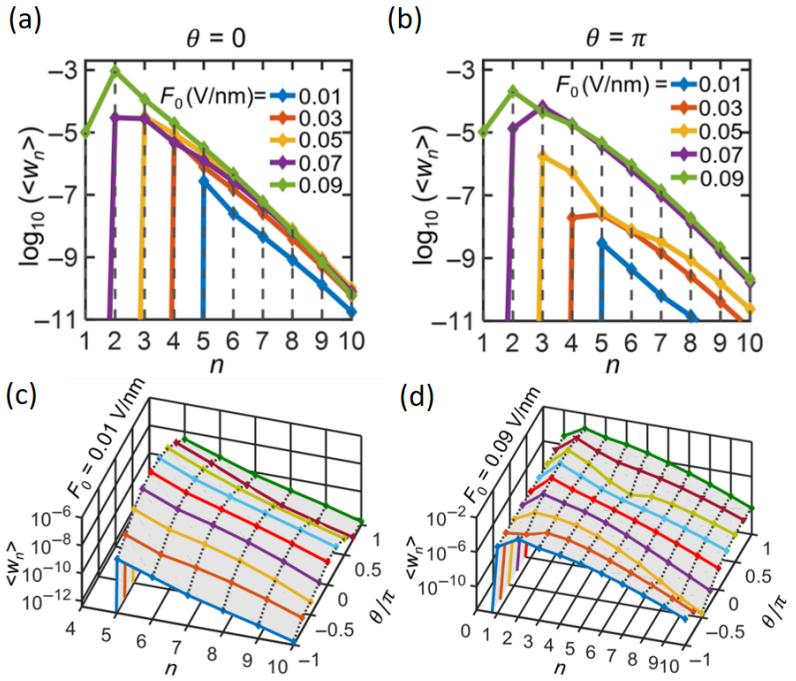

Fig. 2. (a), (b) Time-resolved photoelectron energy spectra for the tungsten nanotip due to two-color laser fields $F_1\cos(\omega t)$ and $F_2\cos(2\omega t+\theta)$, for various dc fields, F_0, when (a) $\theta = 0$, and (b) $\theta = \pi$. (c), (d) Photoelectron spectra at different θ for the dc fields (c) $F_0 = 0.01$ V/nm and (d) $F_0 = 0.09$ V/nm. The fundamental laser (1560 nm) field $F_1 = 1.8$ V/nm and the second-harmonic laser field $F_2 = 0.3$ V/nm [2].

c. Interference modulation of photoemission driven by two lasers of the same frequency

We proposed to utilize two lasers of the same frequency to modulate the photoelectron emission by their phase delay [3]. Compared to the two-color laser configuration, single-frequency laser pairs can be more easily implemented in experiments since they relax the requirement of higher order harmonic generation, which becomes increasingly difficult in the high laser intensity regimes. The intensity ratio of the single-frequency laser pairs can be tuned over a much wider range than the two-color laser system. Using a quantum mechanical model, we studied the time-resolved photoelectron energy spectra and emission current modulation under different laser and dc fields. We find that a strong current modulation (> 90%) can be achieved with a moderate ratio of the laser fields (< 0.4) even under a strong dc bias (Fig. 3). The nonlinear effects of the dc field, cathode materials, and laser wavelength on both the emission current level and modulation depth are examined. The strong dependence of photoelectron energy spectra on the phase delay of the two lasers demonstrates promising potential for the application of time-resolved photoelectron spectroscopy using single-frequency laser pairs. Our study may inspire new routes toward many applications requiring both high photoemission current and strong current modulation, such as tabletop particle accelerators, photoelectron microscopy, and x-ray sources.

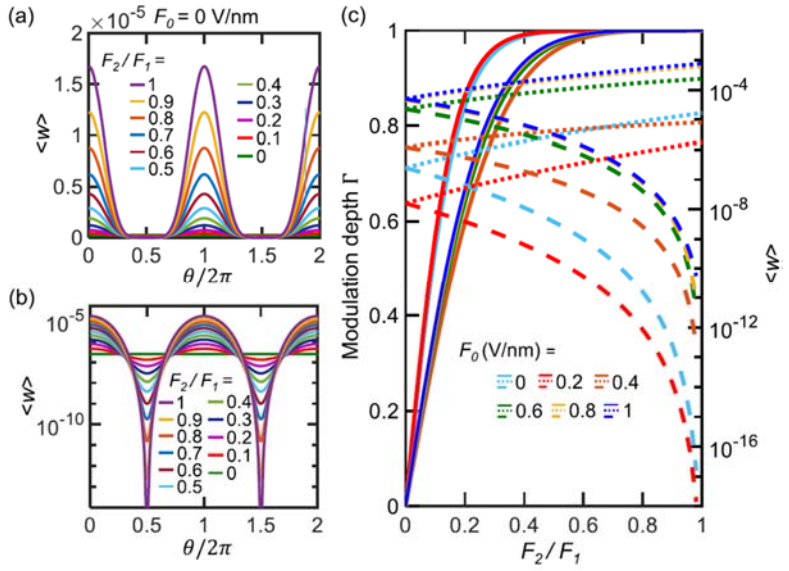

Fig. 3. Photoemission current modulation due to two lasers of the same frequency with electric fields F_2 and F_1 and a phase delay of θ. (a) Normalized total time-averaged emission current density $\langle w \rangle$ as a function of phase difference θ for different F_2/F_1, when the dc field $F_0 = 0$. (b) Semilog plot of $\langle w \rangle$ in (a). (c) Current modulation depth Γ (solid lines) as a function of the laser field ratio F_2/F_1 for different dc fields F_0. Dotted (dashed) lines in (c) are for the maximum (minimum) emission current density $\langle w \rangle$ at $\theta = 0$ ($\theta = \pi$). Here, the laser field F_1 is fixed as 1.8 V/nm. [3].

d. Few-cycle optical-field-induced photoemission from biased surfaces

A variety of models have been developed to understand the underlying emission mechanisms, such as perturbative theory, Floquet models, Fowler-Nordheim tunneling approximation, and directly solving the TDSE. To explicitly reveal the interplay of various emission processes under different regimes and to systematically characterize the parametric scalings of photoemission characteristics, an exact quantum model under ultrashort pulsed condition is highly desirable.

We developed an exact quantum theory on few-cycle optical-field-induced photoemission from biased surfaces [4]. Our exact theory for photoemission due to pulsed lasers is based on the analytical solution of time-dependent Schrödinger equation (TDSE), which is valid for arbitrary pulse length from sub-cycle to CW excitation. Our solution is valid from the photon-driven regime to the optical-field-driven regime, and is applicable for arbitrary laser parameters (i.e., intensity, pulse duration, carrier frequency, and carrier envelope phase (CEP)), dc bias, and metal properties (i.e., work function and Fermi level). The model is also applicable to a train of laser pulses with arbitrary pulse repetition rate (Fig. 4).

In Fig. 5, we plot the normalized total time-dependent photoemission current density $w(\bar{x}, t)$, including oscillatory surface currents, as a function of the space $\bar{x}$ and time t under different dc bias. It is found that increasing the dc field from $F_0 = 1 \times 10^4$ V/m to 1×10^9 V/m increases the normalized time-averaged emission current density from $\langle w \rangle = 2.5 \times 10^{-11}$ to 2.1×10^{-7}. More

importantly, the emission current pulse is significantly shortened (from 19.7 fs to 4.8 fs of FWHM at $\bar{x} = 50$). This may provide a practical way to shorten the photoemission current pulse by simply adding a large dc bias.

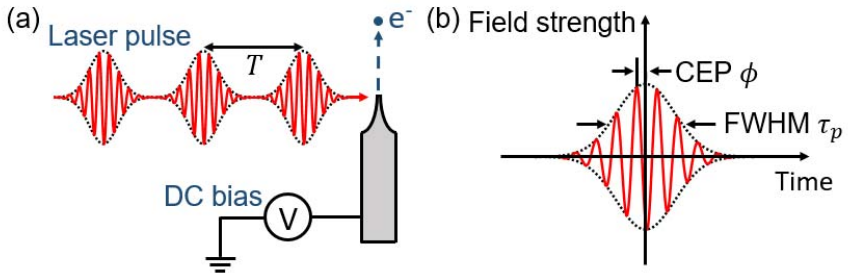

Fig. 4. (a) Sketch of photoelectron emission from a biased emitter under the illumination of a laser pulse train with a time period *T*. (b) A single laser pulse with carrier-envelope phase (CEP) ϕ and full width at half maximum (FWHM) of the field envelope τ_p. The red curve and black dotted lines denote the time evolution of laser electric field and laser pulse envelope, respectively. [4]

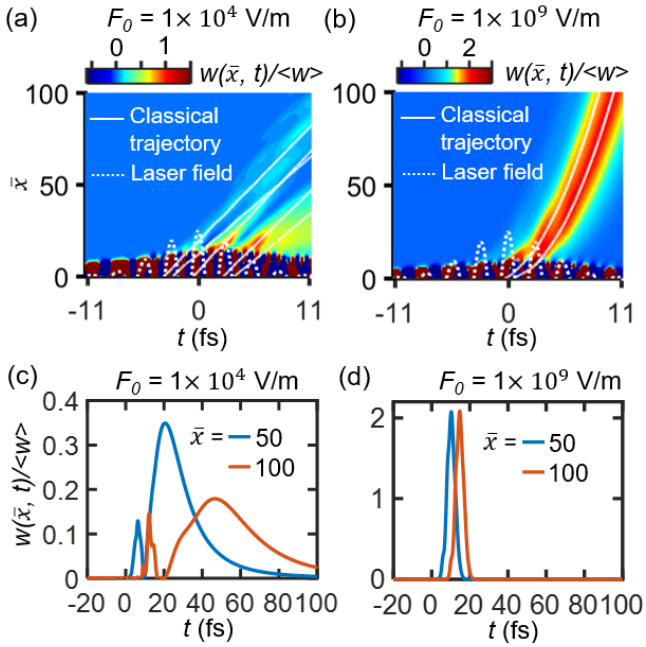

Fig. 5. Total time-dependent emission current density *w(x̄, t)* under the dc field $F_0 = 1 \times 10^4$ V/m and 1×10^9 V/m. (a),(b) *w(x̄, t)* including surface oscillation currents as a function of the space $\bar{x}$ and time *t*. Solid white lines show the corresponding classical trajectories. Dotted white lines show the positive half cycles of the laser electric field. (c),(d) Emission current density *w(t)* at $\bar{x} = 50$ and 100, as a function of time *t*. The time-dependent current in all figures is normalized in terms of the time-averaged emission current $\langle w \rangle$. Here, the laser pulse duration $\tau_p = 8.8$ fs and the peak laser field $F_1 = 1$ V/nm. When $F_0 = 1 \times 10^4$ V/m, $\langle w \rangle = 2.5 \times 10^{-11}$; When $F_0 = 1 \times 10^9$ V/m, $\langle w \rangle = 2.1 \times 10^{-7}$. [4]

e. Photoemission in a nanogap

By exactly solving the TDSE, we constructed an analytical solution for nonlinear photoelectron emission in a nanoscale metal–vacuum–metal junction driven by a laser field (Fig. 6) [5]. We examine the photoelectron energy spectra and emission current under various laser fields and vacuum gap distances. Our calculation shows the transition from direct tunneling to multiphoton induced electron emission as gap distance increases. We find that decreasing the gap distance (before entering the direct tunneling regime) tends to extend the multiphoton regime to higher laser intensity.

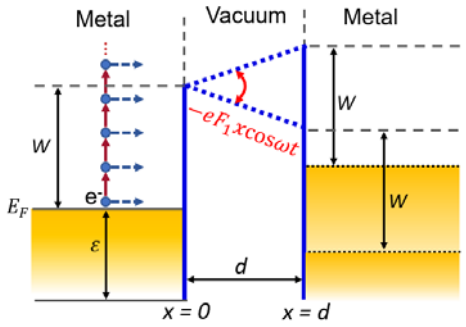

Fig. 6. Energy diagram for photoelectron emission in a nanoscale metal-vacuum-metal junction under a single-frequency laser field. Electrons with the initial energy ε are emitted from the surface at $x = 0$, with an energy of $\varepsilon + n\hbar\omega$, due to n-photon contribution. [5]

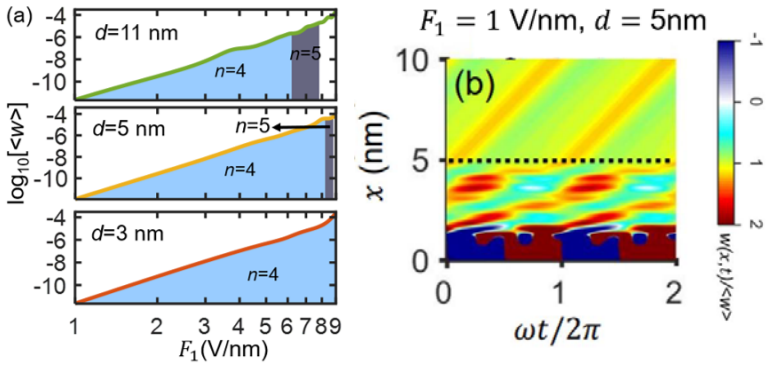

Fig. 7. (a) Normalized total time-averaged emission current density $\langle w\rangle$ as a function of F_1 for d = 3, 5, and 11 nm. Here, laser field regimes are labeled with n = 4 and n = 5 (cf. the areas filled with different colors), meaning the dominant emission process here is four- or five- photon absorption; (b) Total time-dependent current density $w(x,t)$ as a function of time t and space x, under F_1 = 1 V/nm and d = 5nm. Here, $w(x,t)$ is normalized in terms of the time-averaged $\langle w\rangle$. The dotted line is at $x = d$. [5]

Our calculations show that the transition location between the dominant four- and five- photon absorption shifts to larger laser field F_1 for smaller gap distance d (Fig. 7a). This indicates that decreasing the gap distance (before entering the direct tunneling regime) can extend the multiphoton regime to higher laser intensity. This may be explained by the fact that the shape of the potential barrier becomes less sensitive to the laser field strength for a smaller gap distance,

thus allowing the dominant n-photon process to remain over a larger range of laser fields (or laser intensities).

Figure 7b shows the time-dependent current density $w(x,t)$ as a function of space x and time t. It is seen that, besides the surface oscillation current near the metal-vacuum interface at $x = 0$, some electrons are back reflected from the vacuum-metal interface at $x = d$ into the vacuum gap. The full width at half maximum (FWHM) of the emission current pulse is about 0.63 fs, which is greatly shorter than laser period of 2.67 fs.

This work provides clear insights into the underlying photoemission mechanisms and spatiotemporal electron dynamics of ultrafast electron transport in nanogaps and may guide the future design of ultrafast nanodevices, such as photoelectron emitters, photodetectors, and quantum plasmonic nanoantennas.

We have published this work in Applied Physics Letters [5]. It was selected as a Featured article.

3.1.2 Plasmon-enhanced resonant photoemission using atomically thick dielectric coatings

Despite extensive research exploring efficient multiphoton absorption at low laser intensities or optical field tunneling at high laser intensities, the use of photoemission from nanotips is still limited by its low emission current and low quantum efficiency.

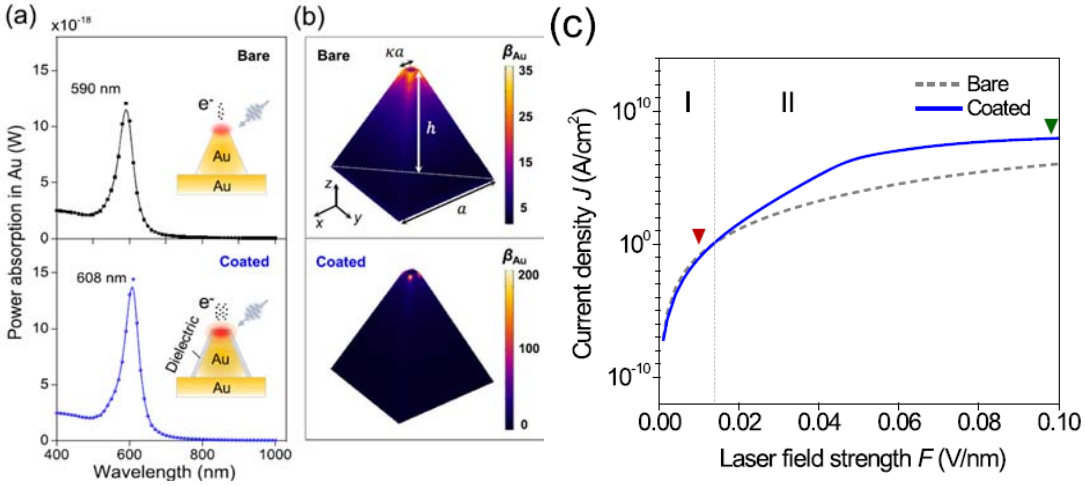

Fig. 8. Resonant photoemission. (a) Schematic of the resonant photoemission from either bare or coated Au-nanopyramid field emitters (insets) with their simulated plasmon resonances. (b) Corresponding simulated resonant field enhancements β_{Au} at the Au surface. In the simulation, the nanopyramid has fixed side length a = 40 nm, height h = 40 nm, and aspect ratio κ = 0.1. It is either bare or coated with a dielectric layer with thickness d = 1nm and refractive index n = 1.5. (c) the photoemission current density J as a function of the field strength of the incident laser F, for the bare or coated photoemitters. [6].

We studied the enhancement of photoemission by coating metal nanoemitters with an atomically thick dielectric [6]. The thin coating is able to enhance the local optical field near the emitter tip

through plasmonic resonance, where optical field tunneling can be accessed at a significantly reduced incident laser intensity. The physics behind this effect lies in the considerably enhanced plasmon resonant fields highly confined within the dielectric coating (in addition to the geometrical plasmon field enhancement) and the lowered tunneling barrier due to the electron affinity. We performed optical simulations and employed our quantum photoemission model to investigate the photoemission processes under the plasmon resonant conditions on both bare and coated Au-nanopyramid field emitters (Fig. 8). The proposed mechanism is independent of the geometry of the metal nanoemitter, and practically the coating could protect the metal nanoemitters from corrosion or metal atom migration under intense optical fields. The ideas presented in this work may result in the fabrication of strong-field photoemitters with higher yields and longer lifetimes.

The work is published in ACS Nano [6]. A US patent is filed for enhancing photoemission using atomic thick dielectric coating [7].

3.1.3 Quantum efficiency from the exact quantum photoemission model

a. Quantum efficiency under different laser intensities

Our quantum mechanical model for photoemission from a metal surface due to the excitation of laser electric fields was applied to study the quantum efficiency (QE). The quantum model includes the effects of laser fields (wavelength and intensity), properties of metals (Fermi energy and work function including Schottky effects), and the applied dc field on the cathode surface [8].

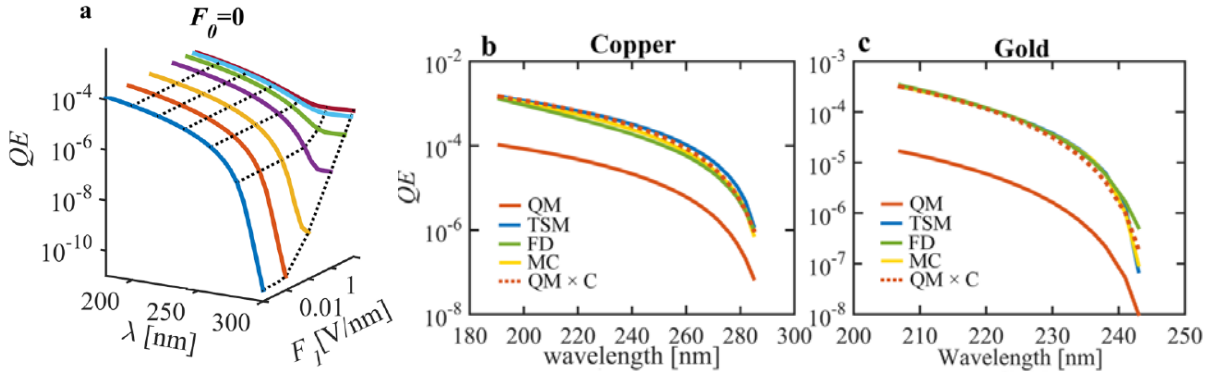

Fig. 9. (a) Quantum efficiency (QE) calculated based on our quantum model, under various laser fields F_1 for the special case of dc fields $F_0 = 0$ in the laser wavelength range of $\lambda = 180 \sim 300$nm. (b) and (c) QE from the quantum model (QM), the three-step model (TSM), the Monte Carlo (MC) simulation based on TSM, the Fowler–DuBridge model (FD), and the fitted QM × C (C = 13.963 and 19.142 for copper and gold, respectively) [8]**.**

We found shorter wavelength lasers can induce more photoemission from electron initial energy levels further below the Fermi level, and therefore yield a larger quantum efficiency (Fig. 9). The dc field increases the quantum efficiency, but it is found to have a greater impact on lasers with

wavelengths close to the threshold (i.e. the corresponding photon energy is the same as the cathode work function) than on shorter wavelength lasers. The quantum model is compared with existing classical models, i.e. three-step model, Fowler-Dubridge model, and Monte Carlo simulation. Even though with very different settings and assumptions, it is found that the scaling of the quantum efficiency of the quantum model agrees well with the other models for low intensity laser fields. When the laser field increases, QE increases with the laser field strength in the longer laser wavelength range due to the increased contributions from multiphoton absorption processes.

A comprehensive paper on the quantum efficiency from our quantum model is published in Journal of Applied Physics [8]. It is selected as an Editor's Pick article.

b. Quantum efficiency with laser wavelengths from UV to NIR

Most recently, we applied our quantum model to study photoelectron emission from metal surfaces with laser wavelengths from 200 to 1200 nm (i.e., ultraviolet to near-infrared). The dominant electron emission mechanism varies from different multiphoton emission processes to dc or optical field emission, depending on the laser intensity, wavelength, and dc bias field. The parametric dependence of QE is analyzed in detail. It is found that QE can be increased nonlinearly by the non-equilibrium electron heating produced by intense sub-picosecond laser pulses. This increase of QE due to laser heating is the strongest near laser wavelengths where the cathode work function is an integer multiple of the corresponding laser photon energy. The quantum model, with laser heating effects included, reproduces previous experimental results, which further validates our quantum model and the importance of laser heating.

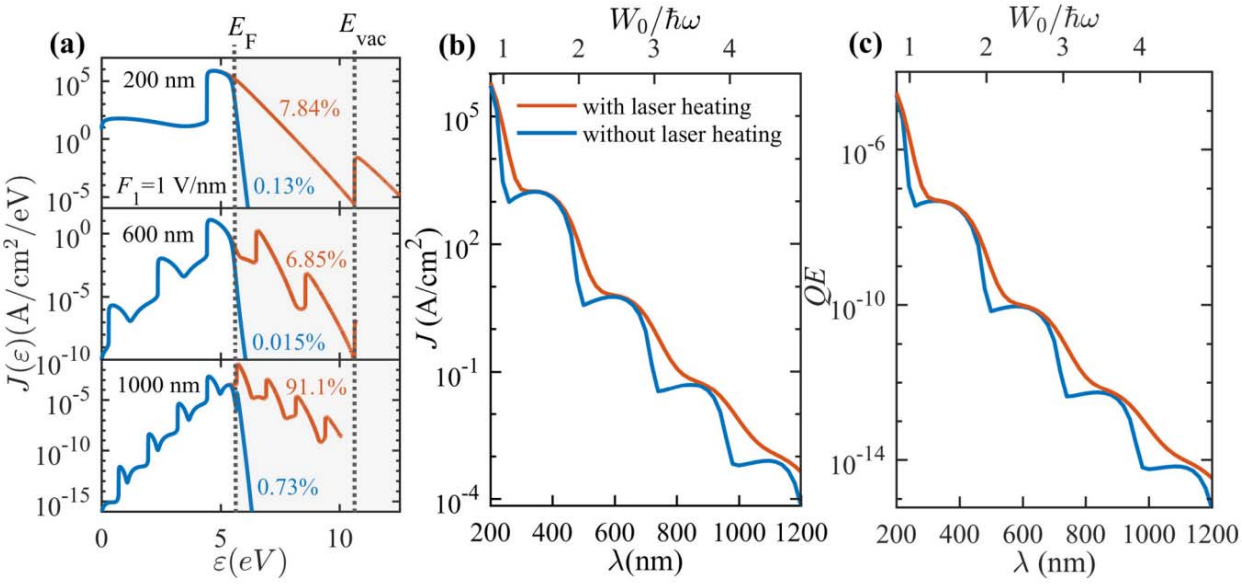

Fig. 10. Laser heating effects on photoemission. (a) Electron emission current density per electron initial energy for $\lambda = 200$ nm, 600 nm, and 1000 nm, with laser field $F_1 = 1$ V/nm and dc field $F_0 = 0$; (b) Electron emission current density and (c) QE as a function of laser wavelength for $F_1 = 1$ V/nm and zero dc field $F_0 = 0$. [9]

Figure 10 shows a comparison of photoemission with laser heating effects (red curves) and without laser heating effects (blue curves, with $T = T_e \equiv 300\text{K}$). The electron emission current density per electron initial energy, $J(\varepsilon)$, extends to energy levels above the Fermi level as the laser heating effect is considered, as shown in Fig. 10(a). Figure 10(b) shows the emission current density as a function of the laser wavelength. The quantum efficiency as a function of laser wavelength is shown in Fig. 10(c), showing the same trend as J vs. λ in Fig. 10(b). In summary, the increase of QE due to laser heating is the strongest near the step points (i.e. ratio of work function over photon energy $W_0/\hbar\omega =$ integer) and is more profound for longer laser wavelengths.

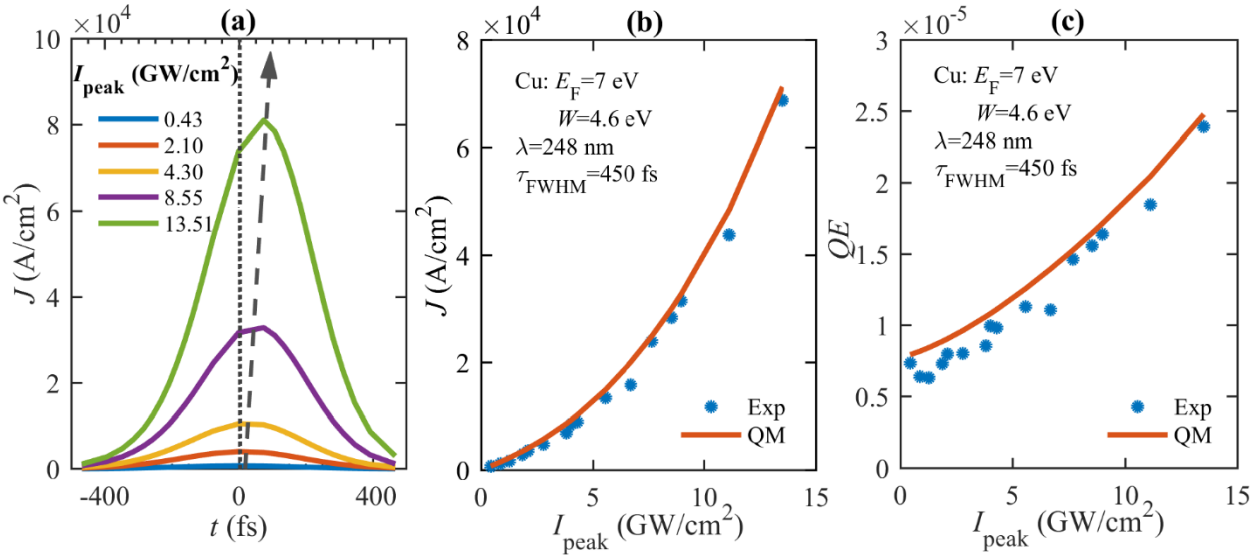

Fig. 11. Comparison with experimental results. (a) Calculated emission current density temporal profile for various laser intensities used in the experiment [9]**. (b) Emission current density as a function of the peak laser intensity. Scatters are experimental data extracted from N. A. Papadogiannis, S. D. Moustaïzis, and J. P. Girardeau-Montaut, J. Phys. D: Appl. Phys. 30, 2389 (1997). The red curve is calculated by our quantum model. (c) Quantum efficiency as a function of the peak laser intensity.** [9]

We demonstrate the validity of the above quantum model with laser heating, by comparing it with experimental results in N. A. Papadogiannis, S. D. Moustaïzis, and J. P. Girardeau-Montaut, J. Phys. D: Appl. Phys. 30, 2389 (1997). In the experiment, a laser pulse of 450 fs duration at 248 nm is used. The metal is copper, with Fermi energy $E_F = 7$ eV and work function $W_0 = 4.6$ eV. The temporal profile of the emission current density is shown in Fig. 11(a). The calculated current density by the quantum model is shown as red curve in Fig. 11(b), which is in good agreement with the experimental measured current density shown as blue scatter points. The quantum efficiency is plotted in Fig. 11(c). It is clear that QE increases with the laser intensity instead of being constant (as predicted in Einstein's photoelectric effect), which is ascribed to the laser heating induced electron redistribution.

The work on QE for lasers from UV to NIR is also published in Journal of Applied Physics [9]. The paper is selected as a Featured article, and is highlighted in Scilight, and reported by news in Phys.org and MSUToday.

3.1.4 Field emission from CNT fibers and CNT fiber array cathodes

a. Field emission from CNT fibers in varying anode-cathode gap with the effects of contact resistance

We studied field emission (FE) from a single carbon nanotube (CNT) fiber with different anode-cathode (AK) gap distances [10]. The experiments are conducted by Dr. Steve Fairchild's group of AFRL Wright-Patterson. It is found that the field enhancement factor depends strongly on the finite AK gap distance, due to the combination of geometrical effects and possible fiber morphology change. The geometrical effects of AK gap distance on the field enhancement factor are confirmed using COMSOL simulations. The slope drop in the Fowler-Northeim (FN) plot of the FE data in the high voltage is related to the electrical contact resistance between the CNT fiber and the substrate (Fig. 12). It is found that even a small series resistance to the field emitter (<30% of the emission gap impedance) can strongly modify the FE characteristics in the high voltage regime, inducing a strong deviation from the linear FN plot.

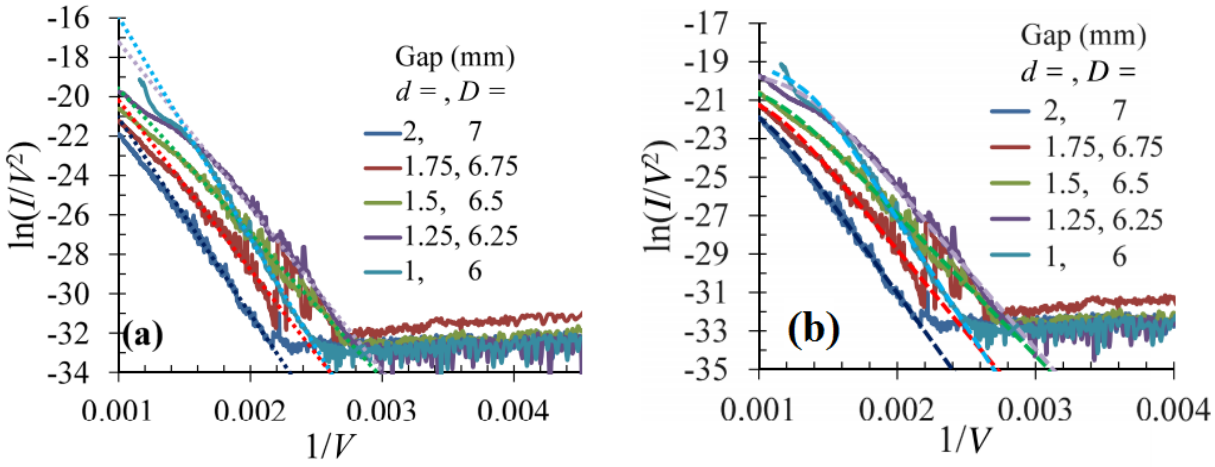

Fig. 12. Curve fitting (broken lines) to the field emission data (solid lines), (a) without including a series resistance, (b) with including the effects of a series resistance. [10]

b. Field emission from carbon nanotube (CNT) fiber array cathodes

We studied field emission (FE) field emission from carbon nanotube (CNT) fiber array cathodes [11]. The Fowler-Nordheim theory was used to calculate the effective field enhancement factor values for field emission array (FEA) cathodes comprised of multiple CNT fibers arranged in various array configurations, developed at AFRL. Electrostatic simulations

were performed using COMSOL Multiphysics modeling software to model the field enhancement of a perfectly uniform 5×5 array (Fig. 13). The effective field enhancement factor (β_{eff}) for the total array was compared to the individual field enhancement values at the fiber tips predicted by a surface potential model that predicted the field amplification of all 25 CNT fibers in the array.

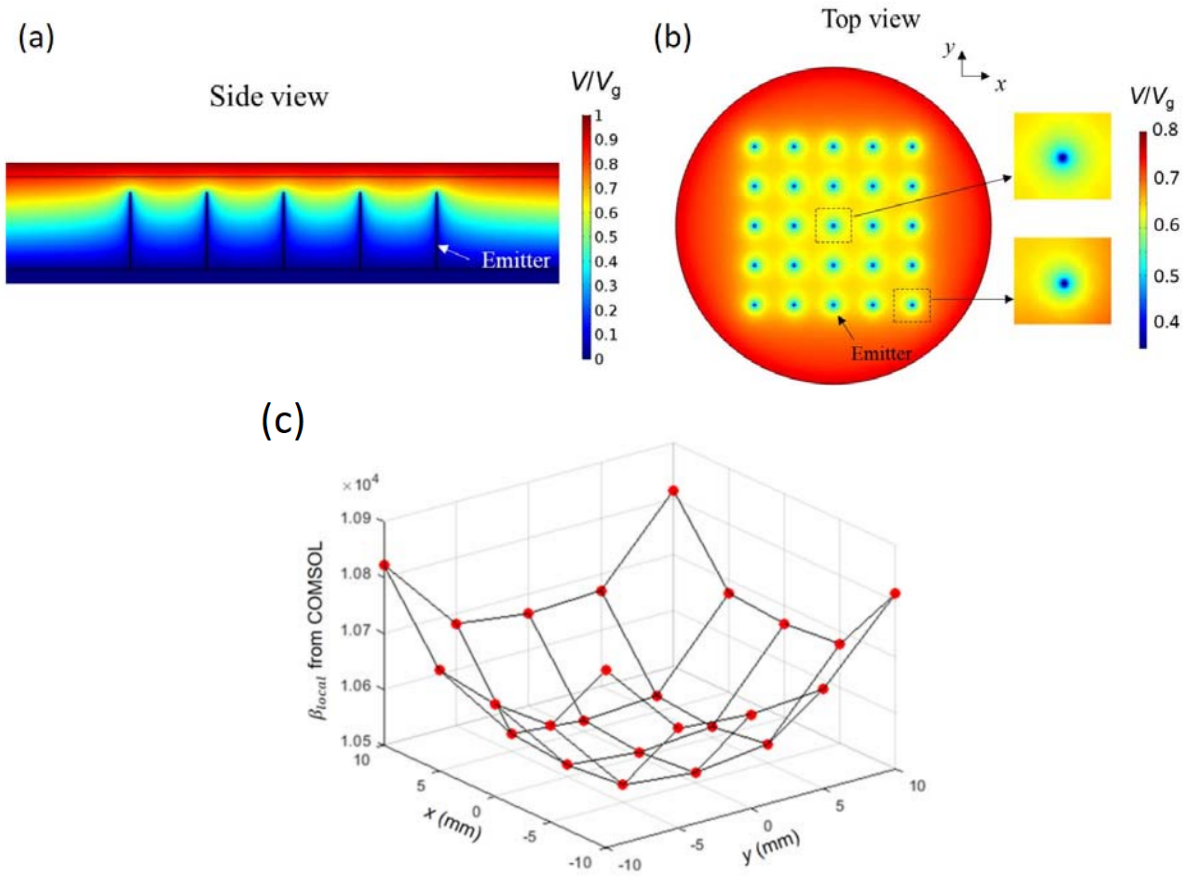

Fig. 13. (a) Side view and (b) top view of the potential profile of the 5 × 5 FEA cathode calculated from COMSOL, (c) the corresponding local electric field enhancement factor of the fibers, $\beta_{\text{local}} = E_{\text{local}}/E_0$, defined as the ratio of the local vacuum electric field at the center of the top surface of each tip E_{local} over the applied electric field $E_0 = V_g/D$, where V_g is the applied voltage, and D is the gap distance. [11]

3.1.5 Generalized tunneling model in dissimilar metal-insulator-metal junctions

Quantum tunneling is important to nanoelectronic circuit designs, tunneling electrical contacts, scanning tunneling microscopes (STMs), plasmonic resonators, carbon nanotubes, graphene and other two-dimensional (2D) materials based devices, and novel vacuum nano-devices. Quantum tunneling effects impose serious challenges to the physical scaling down of traditional electronic circuits. On the other hand, it enables the development of future tunneling field-effect transistors (TFETs), which are envisioned to further extend Moore's law.

We studied the current density-voltage ($J-V$) characteristics of dissimilar metal-insulator-metal (MIM) nanoscale tunneling junctions using a self-consistent quantum model [12]. The model includes emissions from both cathode and anode, and the effects of image charge potential, space charge and exchange correlation potential. The $J-V$ curves span three regimes: direct tunneling, field emission, and space-chargelimited regime. Unlike similar MIM junctions [P. Zhang, Sci. Rep, 5, 9826 (2015)], the $J-V$ curves are polarity dependent (Fig. 14). The forward (higher work function metal is negatively biased) and reverse (higher work function metal is positively biased) bias $J-V$ curves and their crossover behaviors are examined in detail for various regimes, over a wide range of material properties (work function of the electrodes, electron affinity and permittivity of the insulator). It is found that the asymmetry between the current density profiles increases with the work function difference between the electrodes, insulator layer thickness and relative permittivity of the insulator. This asymmetry is profound in the field emission regime and insignificant in the direct tunneling, and space charge limited regimes.

This is the most general scaling law for tunneling current to date [12].

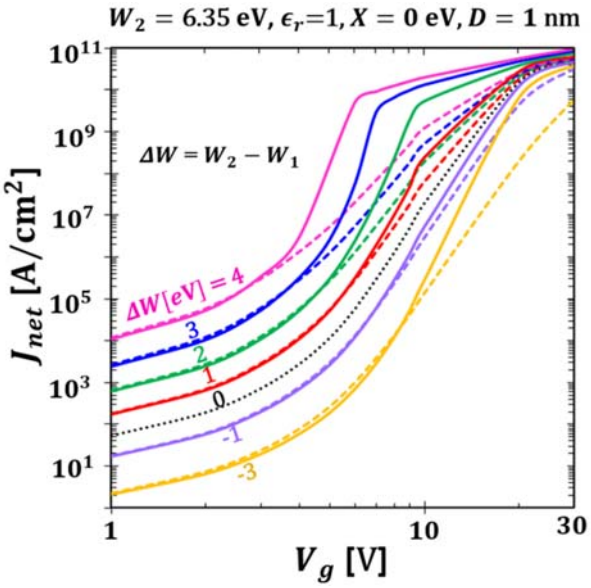

Fig. 14. The effects of work function difference ΔW on the $J-V$ characteristics of a dissimilar MIM junction with D = 1 nm, vacuum gap (ϵ_r = 1, X = 0 eV). The work function of metal 2 is kept fixed, W_2 = 6.35eV (Pt). Solid and dashed lines represent reverse biased (RB) and forward biased (FB) conditions respectively [12]**.**

3.1.6 Secondary electron emission reduction in porous surfaces

Secondary electron emission (SEE) causes performance degradation in rf accelerators, microwave components, and satellite communication systems. In collaboration with AFRL, University of Cincinnati, and Univeristy of Cambridge, we investigated secondary electron yield (SEY) mitigation from a metal surface with a micro-porous array fabricated using laser drilling technique [13].

We proposed a general empirical model to fit the experimentally measured SEY of a flat gold surface for normal and oblique incidence of primary electrons. Using this empirical model, we developed a two-dimensional Monte Carlo (MC) simulation scheme to determine the effective SEY of a micro-porous array. It is found that the SEY from a porous surface is significantly reduced compared to that of the flat surface. By taking into account all the generations of secondary electrons inside a porous well, our MC results are found to be in very good agreement with the experimental data (Fig. 15). The dependence of the SEY on the aspect ratio of the micropores and porosity of the surface is examined. A simple empirical formula has been proposed to evaluate the effective SEY of the gold micro-porous array for pores of arbitrary aspect ratio.

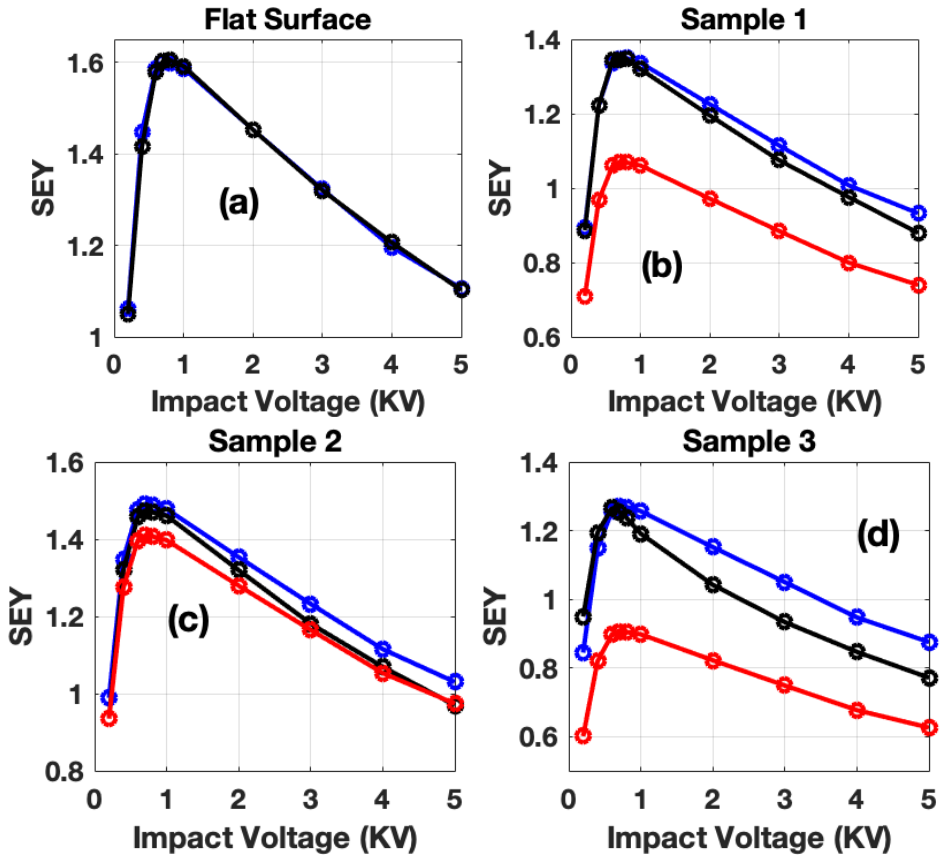

Fig. 15. Comparison of experimental measurements (black lines), previous analytical predictions (red lines), and MC simulations (blue lines) of SEY for normal incidence on microporous gold surface with different pores aspect ratio, A_R and surface porosity, ρ: (a) flat surface with $A_R = 0, \rho = 0$, (b) sample 1 with $A_R = 3.025, \rho = 0.395046$, (c) sample 2 with $A_R = 3.025, \rho = 0.142216$, and (d) sample 3 with $A_R = 3.524, \rho = 0.5044$. [13]

The study was later extended for ablique incidence of primary electrons onto a porous surface (Fig. 16) [14]. Our proposed general SEY model is valid for arbitrary angular dependence, materials, and surface morphologies [14].

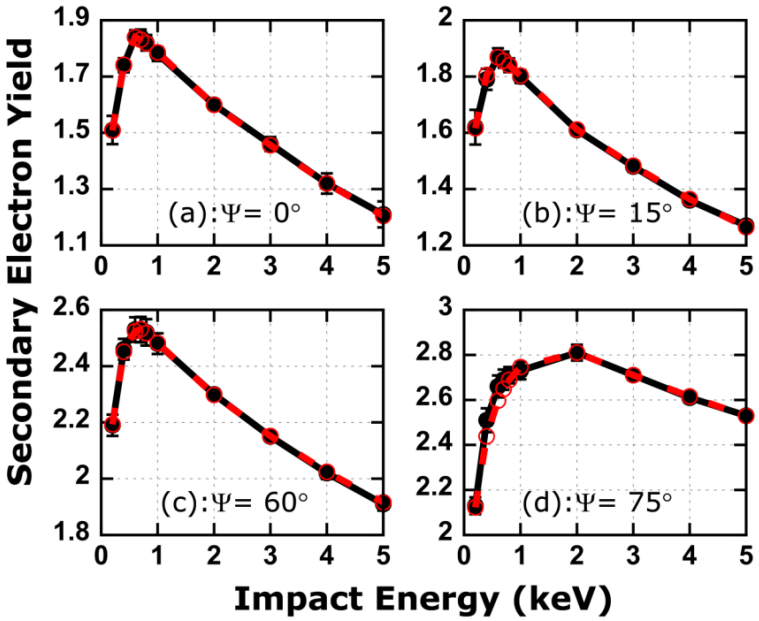

Fig. 16. Measured secondary electron yield compared to our empirical model of a flat (nonporous) gold surface for primary electron incidence angles of (a) ψ = 0°, (b) ψ = 15°, (c) ψ = 60° and (d) ψ = 75°. The measured results and empirical fits are represented by solid black lines and dashed red lines, respectively [14].

3.1.7 Theory of field emission from dielectric coated surfaces

We studied field emission from dielectric coated surfaces [15]. Common challenges of field emission include the operation requirement of high vacuum condition and current instabilities. To overcome these problems, ultrathin coatings, such as graphene, graphene oxide, and zinc oxide are fabricated onto the emitter to provide chemical and mechanical protection. Coated emitters are demonstrated to not only have longer current stability, but also smaller turn-on electric field and enhanced current emission due to the lowering of the effective potential barrier. In addition to the artificially fabricated coatings, native oxides or foreign adsorbates can be easily formed on the surface of the emitter at low vacuum condition. The thin oxide film or the coated dielectric layer on the cathode surface forms a double-layer potential barrier, which strongly influences the field emission properties. The heterostructure in the emission barrier introduced by the coating also has its potential to change the electrons' mean transverse energy behavior that affects beam quality, which makes it an active area for photoinjectors for future x-ray free electronlasers (XFELs).

We developed a quantum analytical solution for field emission from the dielectric coated cathode surface (Fig. 17), by solving the one-dimensional (1D) Schrödinger equation subject to the double barrier introduced by the coating layer [15]. The solution is applicable for arbitrary electric dc field, cathode properties (i.e., work function and Fermi level), and dielectric coating properties (i.e., dielectric constant, electron affinity, and thickness). It includes not only field emission but also thermionic emission, and can be further extended to include photoemission. The model predicts that for 1D flat surfaces, coatings of small dielectric constant and large

electron affinity tend to enhance the field emission current. The enhancement can be even stronger for higher dimensional sharp emitters.

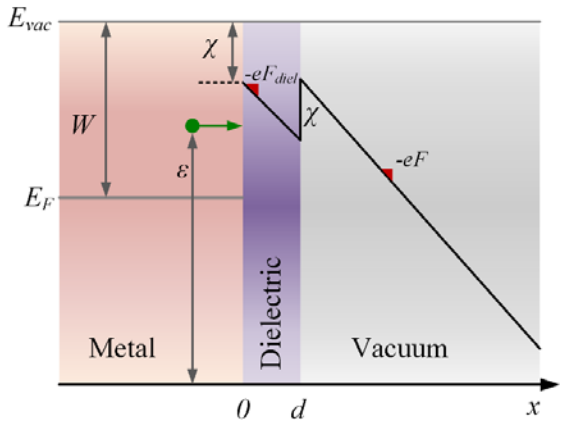

Fig. 17 Field emission from a metal surface coated with a dielectric. The metal-dielectric interface is located at $x = 0$, and the coating's thickness is d. The metal has Fermi level E_F and work function W. The dielectric has electron affinity of χ and dielectric constant of ε_{diel}. The electron initial longitudinal energy is ε. The external dc field of F (in the vacuum) is applied to the emitter surface. The field in the dielectric is $F_{diel} = F/\varepsilon_{diel}$. [15]

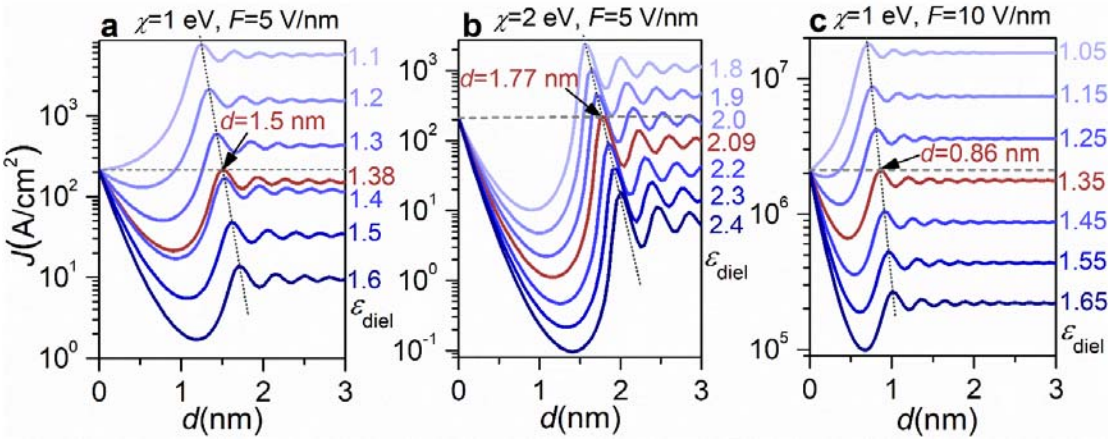

Fig. 18. Emission current density as a function of dielectric thickness d under various dielectric constants ε_{diel} for (a) $\chi = 1\ eV$ and $F = 5$ V/nm; (b) $\chi = 2\ eV$ and $F = 5$ V/nm; and (c) $\chi = 1\ eV$ and $F = 10$ V/nm. The metal is assumed to be gold, with work function $W = 5.1\ eV$ and Fermi energy $E_F = 5.53\ eV$. [15]

Figure 18 shows the emission current density J as a function of dielectric thickness d for various dielectric constant ϵ_{diel}, electron affinity χ, and dc field F. These results can be used to determine the threshold values of dielectric thickness d_{th} and dielectric constant ε_{diel}^{th}, at which the emission current density J is equal to that from the bare metal, for a given dielectric electron affinity χ and dc electric field F. A dielectric constant smaller than ε_{diel}^{th} would enhance the electron emission compared to the uncoated case, with thicknesses corresponding to the curves

above the horizontal dash line. It is found all the three cases in Fig. 18 roughly follow the empirical relation below at room temperature,

$$d_{th}[\text{nm}] = \frac{\varepsilon_{diel}^{th} W}{eF},$$

whose physical origin is due to the change in the potential barrier profiles at this condition.

The work is published in Physical Review Research [15]. Our study provides insights for designing field emitters with higher efficiency and better stability using dielectric coatings.

3.1.8 Perspective on space charge effects in nanodiodes

We published an invited perspective article in Journal of Applied Physics on space charge effects in nanodiodes [16]. This Perspective reviews the fundamental physics of space–charge interactions that are important in various media: vacuum gap, air gap, liquids, and solids including quantum materials. It outlines the critical and recent developments since a previous review paper on diode physics [Zhang et al. Appl. Phys. Rev. 4, 011304 (2017)] with particular emphasis on various theoretical aspects of the space–charge limited current (SCLC) model: physics at the nano-scale, time-dependent, and transient behaviors; higher-dimensional models; and transitions between electron emission mechanisms and material properties. While many studies focus on steady-state SCLC, the increasing importance of fast-rise time electric pulses, high frequency microwave and terahertz sources, and ultrafast lasers has motivated theoretical investigations in time-dependent SCLC. We particularly focus on recent studies in discrete particle effects, temporal phenomena, time-dependent photoemission to SCLC, and AC beam loading. Due to the reduction in the physical size and complicated geometries, we report recent studies in multi-dimensional SCLC, including finite particle effects, protrusive SCLC, novel techniques for exotic geometries, and fractional models. Due to the importance of using SCLC models in determining the mobility of organic materials, this paper shows the transition of the SCLC model between classical bulk solids and recent two-dimensional (2D) Dirac materials. Next, we describe some selected applications of SCLC in nanodiodes, including nanoscale vacuum-channel transistors, microplasma transistors, thermionic energy converters, and multipactor. Finally, we conclude by highlighting future directions in theoretical modeling and applications of SCLC.

Figure 19 illustrates the scope of this Perspective paper: the SCLC in various media and surrounding structures, the manifestation of SCLC in various dynamical and steady-state conditions, and some representative applications of SCLC [16]. In both steady-state and dynamical regimes, SCLC has played a pivotal role in governing the operations of a large variety of applications and devices, ranging from vacuum nanoelectronics, space application, material characterizations, high-power microwave generations, fundamental physics of light-matter interactions, thermionic energy converters (TECs), and many others. These discussions should also provide insights into other applications such as coherent radiation sources, non-neutral charged particle beams, accelerators, and electric propulsion, where space–charge effects on the electron beam are critical.

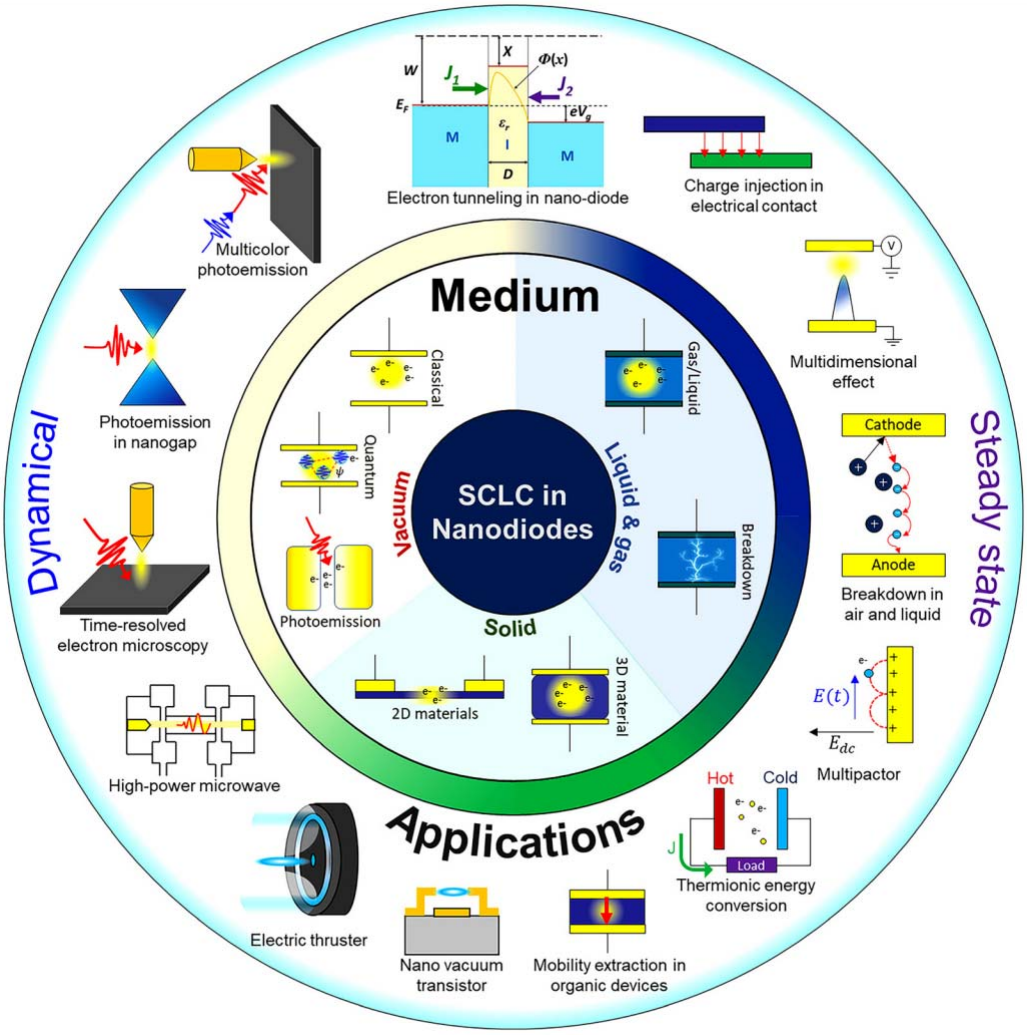

Fig. 19. Schematic overview of space charge limited current (SCLC) in various media, steady-state and dynamical regimes, and several representative applications. SCLC occurs in vacuum, gas, liquid, and solid diodes. SCLC underlies the operations of a large variety of applications, including material characterizations, probing fundamental light-matter interactions, microwave generation, vacuum nanoelectronics, high-power microwave generation, energy conversion, and space technology. [16]

3.1.9 Direct imaging of plasma waves using ultrafast electron microscopy

We introduced a femtosecond plasma imaging modality based on a new development of ultrafast electron microscope [17]. We investigated the laser-induced formation of high-temperature electron microplasmas and their subsequent non-equilibrium evolution (Fig. 20). Based on a straightforward field imaging principle, we directly retrieved detailed information about the plasma dynamics, including plasma wave structures, particle densities, and temperatures. We discovered that directly subjected to a strong magnetic field, the photo-generated microplasmas manifested in novel transient cyclotron echoes and formed new wave states across a broad range

of field strengths and different laser fluences. The transient cyclotron waves morphed into a higher frequency upper-hybrid wave mode with the dephasing of local cyclotron dynamics. The quantitative real-space characterizations of the non-equilibrium plasma systems demonstrate the feasibilities of a new microscope system in studying the plasma dynamics or transient electric fields with high spatiotemporal resolutions.

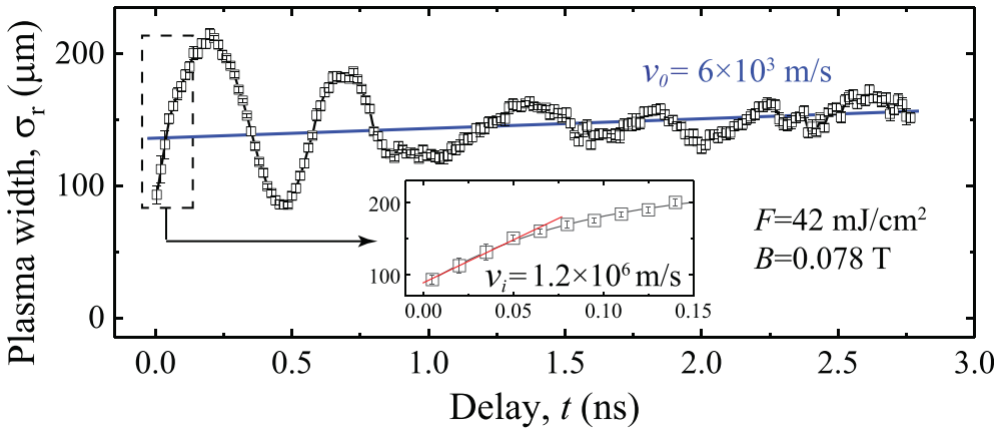

Fig. 20. Plasma profile evolution. Dynamics indicating plasma oscillations, where the blue baseline shows a slow plasma cloud expansion under magnetic confinement. The inset shows the initial space-charge-driven expansion at a much higher velocity. [17]

3.2 Electrical contacts and heating phenomenology

3.2.1 Parallel tunneling electrical contacts

We developed a self-consistent model to characterize partially overlapped parallel contacts with varying specific contact resistivity along the contact length (Fig. 21). For parallel tunneling contacts formed between contacting members separated by a thin insulating gap, we examine the local voltage-dependent variation of potential barrier height and tunneling current along the contact length, by solving the lumped circuit transmission line model (TLM) equations coupled with the tunneling current self consistently [18]. The current and voltage distribution along the parallel tunneling contacts and their overall contact resistance are analyzed in detail, for various input voltage, contact geometry (i.e. contact length, and distance between the contact electrodes), and material properties (i.e. work function, sheet resistance of the contact members, and permittivity of the insulating layer).

It is found the existing 1D tunneling junction models become less reliable when the tunneling layer thickness becomes smaller or the applied voltage becomes larger (Fig. 22). In these regimes, the proposed self-consistent model may provide a more accurate evaluation of the parallel tunneling contacts. The parallel tunneling contact in this work may be considered as the basic building block to better understand the macroscopic electrical conductivity of CNT fibers, which contains a very large number of such parallel contacts between individual CNTs. More importantly, this work provides insights on the design of nanoscale electrical contacts with controlled current distribution and contact resistance via engineered spatially varying contact layer properties and geometry.

The work is published in Scientific Reports [18].

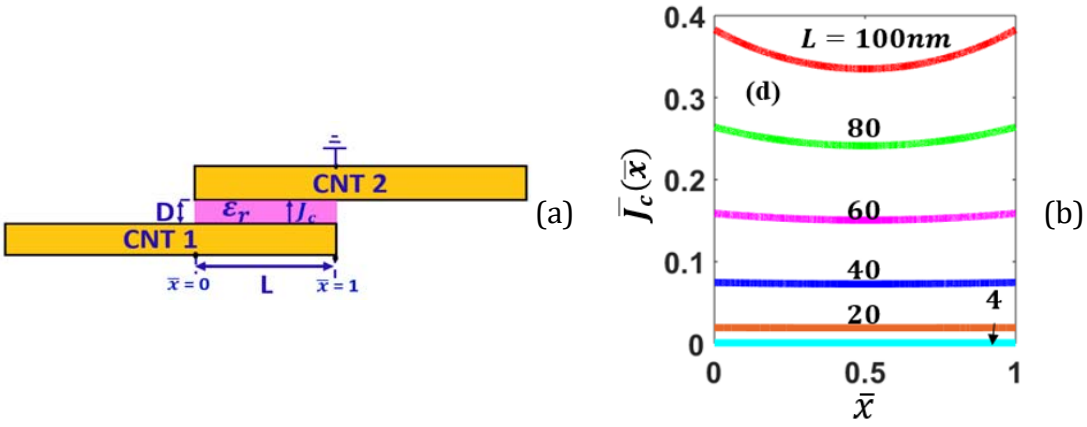

Fig. 21. (a) Parallel contact between two CNTs. A thin (in nm) resistive interface layer of permittivity ε_r and thickness D is sandwiched between them. (b) Normalized (with respect to the input current) tunneling current density from CNT 1 to CNT 2 through the interfacial layer, as a function of $\bar{x} = x/L$, where L is the contact length. Here, the insulator layer is vacuum, with ε_r = 1, electron affinity = 0, and D = 0.5 nm, and L varies from 4nm to 100nm. Work function of CNTs = 4.5 eV, and input voltage = 1V across the two contact ends. [18]

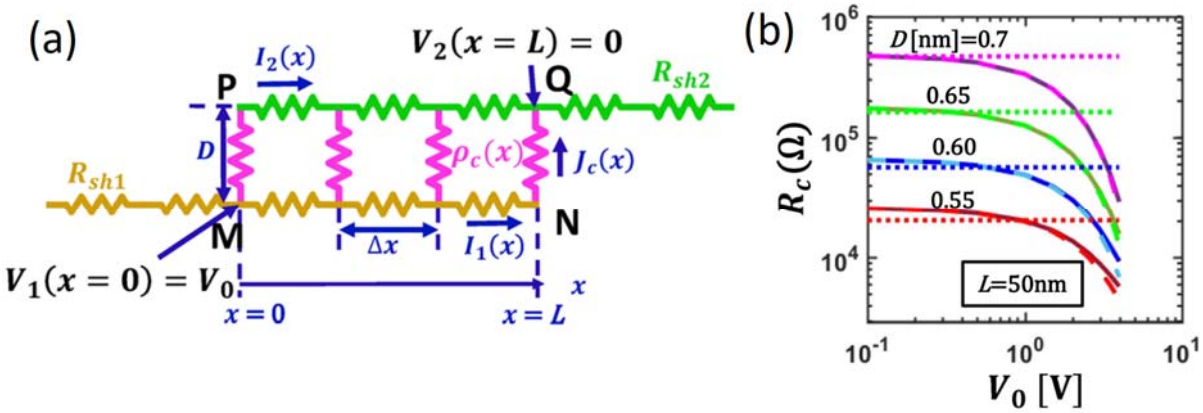

Fig. 22. (a) Transmission line model (TLM) for parallel, partially overlapped electric contact. (b) Contact resistance of CNT-vacuum-CNT contacts as a function of applied voltage V_0 for different contact gap thickness D for contact length L = 50 nm. Solid lines are from our self-consistent TLM, dashed and dotted lines are from 1D models calculated using Simmons formula [J. Appl. Phys. 34, 1793 (1963)] and using ohmic approximations for the tunneling junction, respectively. Here, the insulator layer is vacuum, with ε_r = 1, electron affinity = 0, and work function of CNTs = 4.5 eV. [18]

We extended our recently developed 2D transmission line model to study tunneling type circular thin film contacts [19]. We solved the lumped circuit circular transmission line model (CTLM) with tunneling-induced specific contact resistivity that varies along the radial direction. Our

study shows that the contact resistance is voltage dependent, and the radial current distribution is strongly nonhomogeneous.

3.2.2 Contact modeling for 2D materials, rough interfaces, and irregular contact geometry

We studied the contact resistance and current-flow distribution for electrical contacts between 2D materials and three-dimensional (3D) metals and between different 2D materials [20]. We developed models of the electrical contact resistance for 2D/2D and 2D/3D metal/semiconductor contact interfaces based on a self-consistent transmission-line model coupled with a thermionic charge-injection model for 2D materials, which explicitly includes the variation of the electrostatic potential in the contact region. We compare the results of our self-consistent calculations with existing experimental work and obtain excellent agreement. It is found that the presence of contact interface roughness, in the form of fluctuating Schottky barrier heights in the contact region, can significantly reduce the contact resistance of MoS_2/metal Schottky 2D/3D contacts (Fig. 23). Our findings suggest that roughness engineering may offer a possible paradigm for reducing the contact resistance of 2D-material-based electrical contacts.

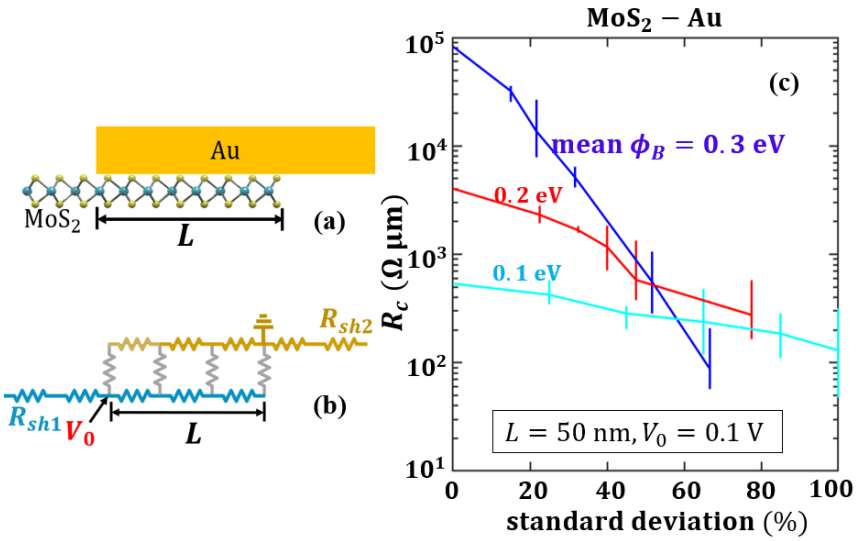

Fig. 23. (a) A parallel, partially overlapped electric contact between monolayer MoS_2 (2D semiconductor) and thin film gold (3D metal); (b) its transmission line model. (c) Contact resistance R_c as a function of interfacial surface roughness (standard deviation/ϕ_B) for different mean values of Schottky barrier height ϕ_B. Here, applied voltage V_0 = 0.1 V, and contact length L=50 nm. [20]

Practical electrical contact edges are irregular either macroscopically due to fabrication errors or microscopically due to the nature of edge or surface roughness. However, electrical contact models typically assume ideal and regular contact geometries, where geometrical effects of the irregular electrode edges are not well characterized. We studied current crowding and spreading resistance of electrical contacts with irregular contact edges. We investigated the scaling of total resistance, spreading resistance, potential drop and current distribution for electrical contacts of tilted contact edges. It is found that for a given edge tilt angle, the scaling of spreading resistance with a follows closely that of zero edge angle [21].

3.2.3 Interface engineering of electrical contacts

Current transport through these contacts greatly influence the device properties and performance. Current crowding can lead to electromigration, localized overheating and the formation of thermal hot spots. To improve efficiency, reliability, and lifetime of the device, it is critical to control the electrical properties in these contact structures. We proposed a method to design nanoscale electrical contacts with controlled current and voltage distribution via engineered spatially varying contact layer properties and geometry (Fig. 24) [22,23].

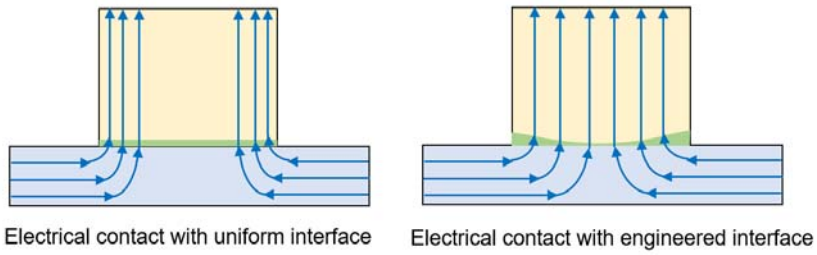

Fig. 24. Spatially engineered contact interface helps mitigate current crowding effect.

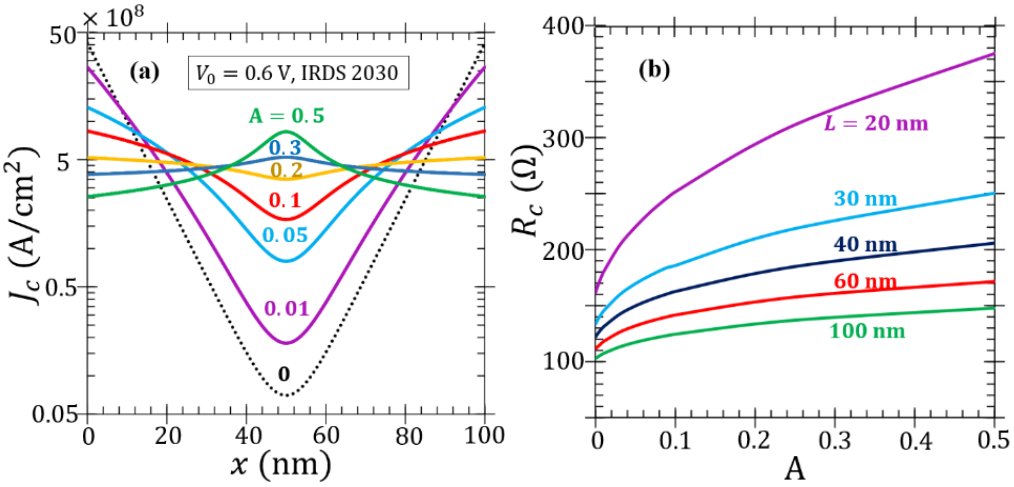

Fig. 25. Engineered ohmic Cu-Cu contact with specific interface contact resistivity $\rho_c(x) = 18 \times 10^{-10}(\mathrm{A}\,(2x/L-1)^2 + 0.01)\ \Omega\ \mathrm{cm}^2$. (a) Contact current density $J_c(x)$ along the contact length for different values of A; (b) contact resistance as a function of A for different contact length L. The input voltage is the required industry standards according to the International Roadmap of Devices and Systems (IRDS) for year 2030. [23]

Figure 25a shows that in similar contacts, current crowding can be greatly decreased by varying the interface contact resistivity ρ_c parabolically along the contact length. We found that for large contact lengths, the change in contact resistance R_c with the parabolic constant A, is not significant, as shown in Fig. 25b. Therefore, the proposed interface engineering method may be

used to eliminate current-crowding effects and achieve uniform contact-current distribution without sacrificing the total current in the circuit [23].

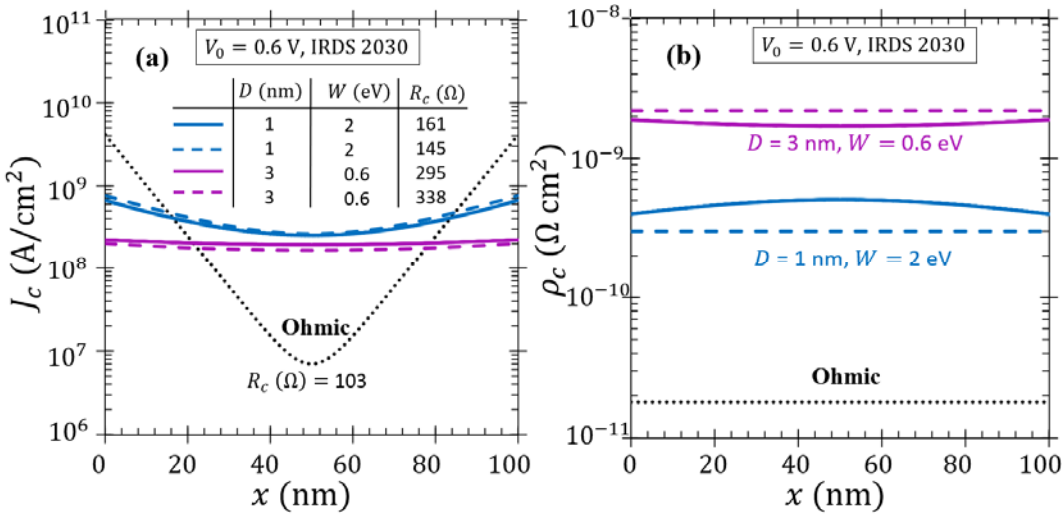

Fig. 26. Tunneling contact engineering. (a) Contact current density $J_c(x)$, and (b) specific contact resistivity $\rho_c(x)$ along the contact length for Cartesian tunneling contacts. Solid lines are for self-consistent numerical calculations, and MIM quantum tunneling formulations. Sheet resistance of both the contact members is assumed to be $R_{sh1} = R_{sh2} = 18\ \Omega/\square$. Dashed lines are calculated analytically with constant ρ_c calculated using gap voltage $V_g = V_0$ in the 1D MIM tunneling model. Black dotted lines are for an ohmic contact with $\rho_c = 1.8 \times 10^{-11}\Omega\ \text{cm}^2$, analytically calculated from the TLM equations. R_c is the total contact resistance. [23]

We proposed another method, *tunneling contact engineering*, to effectively eliminate current crowding in highly conductive ohmic contacts. We introduced a thin (in nm) tunneling layer of thickness (D) and work function (W) between the contact members and compared the profiles of contact current density J_c (Fig. 26) [23]. The interfacial current is much more evenly distributed for contacts with a tunneling layer (colored lines in Fig. 26a). Thus, the nonhomogeneous current distribution in highly conductive contacts can be reduced substantially without significantly increasing the contact resistance (inset in Fig. 26), if the contact members are separated by a thin (in sub-nanometer) insulating tunnelling gap.

Because of the novelty of designing the current distribution and contact resistance via engineered contact layer properties and geometry, this work is issued a US patent on tunneling electrical contacts [22] filed through the Michigan State University patent office.

3.2.4 Coupled electrical-thermal conduction in looped carbon nanotube (CNT) fiber emitters

Because of joule heating, carbon nanotube (CNT) field emitters are heated to high temperatures during field emission. It is important to improve the thermal management of emitters to increase their reliability and prevent premature failure. Collaborating with AFRL Wright-Patterson (Dr. Steve Fairchild's group) and AFRL Kirtland (Dr. N. P. Lockwood), we compared the field

emission characteristics and the temperature distribution of a new configuration of a looped CNT fiber emitter with a traditional single vertical CNT fiber emitter (Fig. 27) [24]. It is found that the maximum temperature of the looped fiber emitter is significantly reduced compared to that of the vertical fiber at the same emission current level. We applied our recently developed theory on the joule heating of a one-dimensional conductor to explain the experimentally measured temperature distributions (Table 1). This study provides new insights into the design of high performance field emitters.

Our paper [24] was selected as a Feature Paper in the journal Applied Sciences.

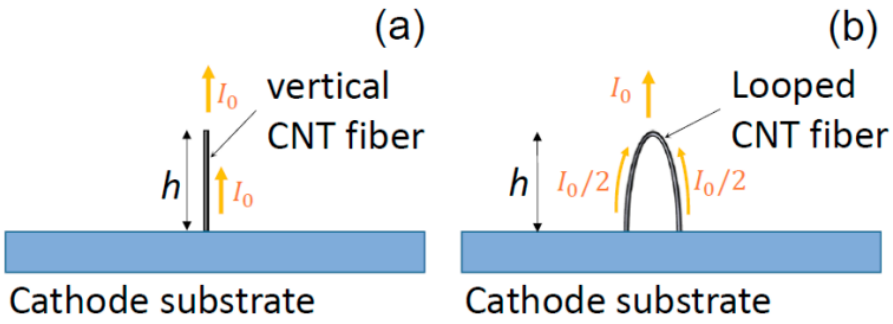

Fig. 27. Schematic of the field emitter configurations (a) single vertical CNT fiber, (b) looped CNT fiber.

Carbon Nanotube (CNT) Fiber Emitter		Measured	Constant σ and κ	Constant σ and Linear $\kappa(T)$	Linear $\sigma(T)$ and Polynomial Fit to $\kappa(T)$
Vertical	T_{max} [°C]	~600	580	595	600
	S_{max} [mm]	~3.0	4	3.5	3.1
Looped	T_{max} [°C]	~300	254	286	300
	S_{max} [mm]	~4	4	4	4

Table 1. Comparison of the measured maximum temperature and its location for both the vertical and looped fiber emitters, with the recent theory under various assumptions [24]**.**

3.3 Electron beam-circuit interaction

3.3.1 Review of recent theory of traveling-wave tubes

We reviewed the recent theory of traveling-wave tubes (TWTs) [25]. This work is in collaboration with Dr. John Luginsland of Confluent Sciences, LLC. The traditional Pierce theory was first briefly reviewed. The classic Pierce theory was then extended in several directions: harmonic generation (from dynamical synchronous interaction between the beam and circuit in an octave bandwidth tube) and beam loading on the circuit (stressing the symmetry between beam and circuit and their coupling) (Fig. 28). Additionally, we have discussed the links

between normal mode analysis associated with coupling individual cavities and its relationship to Pierce theory [25].

This work was published as an invited tutorial paper in Plasma Research Express [25].

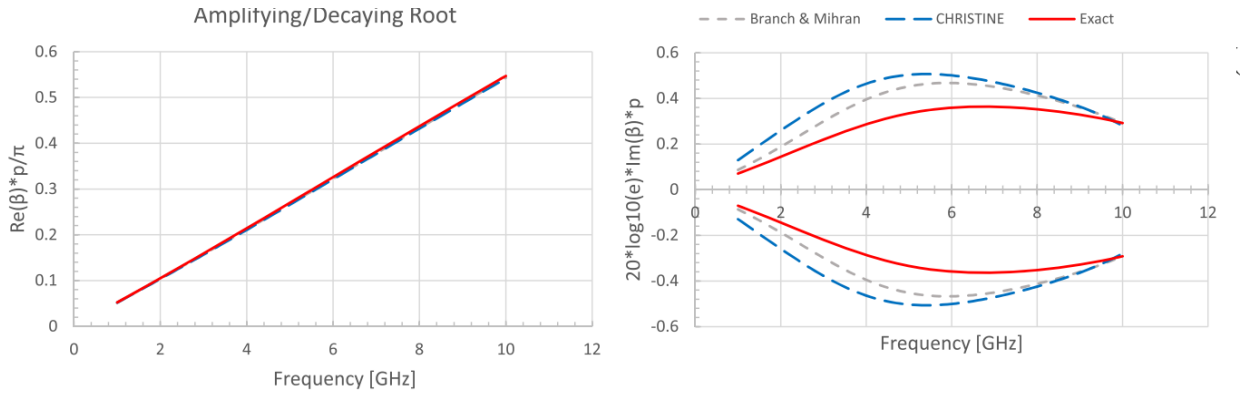

Fig. 28. Plot of the complex roots (propagation constant β) for a TWT as determined from: Pierce theory with Q modeled by Branch and Mihran (gray, dashed), Pierce theory with Q modeled by the sheath helix model as used by CHRISTENE (blue, dashed), and the exact dispersion relation (red, solid) as a function of input signal frequency. [25]

3.3.2 Discrete cavity analysis

Coupled-cavity travelling wave tubes are important to applications which require broad-band amplification and high gain. Classical Pierce theory has treated the beam-circuit interaction being continuous and the tube length being infinite. However, it is important to test the limit of this continuous treatment of beam-circuit interaction in real systems where the tubes are finite and discrete cavity effects may become important. The main motivation behind this study is to obtain a model that allows us to configure the individual cavities' parameters.

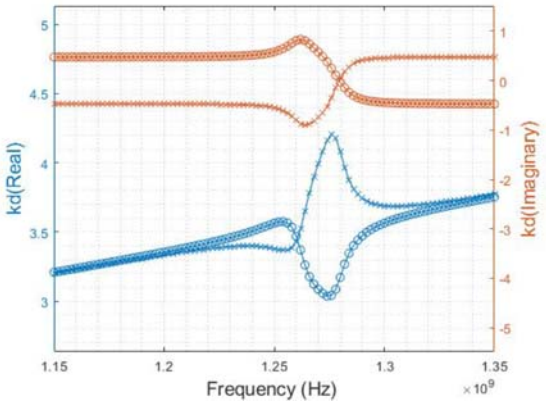

Fig. 29. Hot-tube dispersion relation for a 2 cavity system. In the calculation, we use the quality factor Q = 100, coupling constant c = 0.0112, resonant frequency of individual cavity $\omega_0/(2\pi)$ = 1.27 GHz, impedance Z = 1.6 Ω, beam density $\omega_p = 1.072 \times 10^9$ rad/s, beam velocity $v_0 = 2.48 \times 10^8$ m/s , the cross-sectional area of the beam A = 0.0147 m^2 and the tube length *d* = 11 cm.

Very recently, we extended the previous preliminary work on the discrete cavity model by Wong et al [25]. We studied the effects of coupling in the cavities and demonstrated a hot-tube analysis using the discrete cavity model. Figure 29 examplified a 2 cavity hot-tube results. Two complex roots of k were obtained. It showed evidence of resonance between 1.25 and 1.3 GHz, as expected for the chosen paramters listed in the caption of Fig. 29.

3.3.3 Effects of grating parameters on Smith-Purcell radiation

High-power, efficient, and low-cost electromagnetic sources have significant uses in high-resolution imaging, biomedical scanning, material analysis, security systems, and high-rate data communications, etc. Back wave oscillation (BWO) based Smith-Purcell Radiation (SPR) has attracted strong interests for producing Terahertz (THz) radiation.

Most recently, we calculated the SPR operating points based on dispersion curves at different grating parameters (groove's heights and widths) with a fixed grating period (Fig. 30). According to the SPR equation, the frequency of SPR radiation depends on the period of the metallic grating. Our exact dispersion relationship, on the other hand, shows that the frequency of SPR varies significantly with grating parameters, when SPR occurs at the second harmonic of the operating frequency. We hope to explain this dependence of grating parameters explored in P. Zhang, L. K. Ang, and A. Gover, Phys. Rev. ST Accel. Beams, 18, 020702 (2015), by examining the hot-tube dispersion relation.

In line with these findings, the numerical analysis using CST showed that when the grating is excited with a beam having a bunching frequency close to the SPR frequency calculated from the dispersion relation, the radiation field is significantly higher than when it is excited with other beams of other bunching frequencies. These results may also hold the potential for measuring the properties of electron bunches.

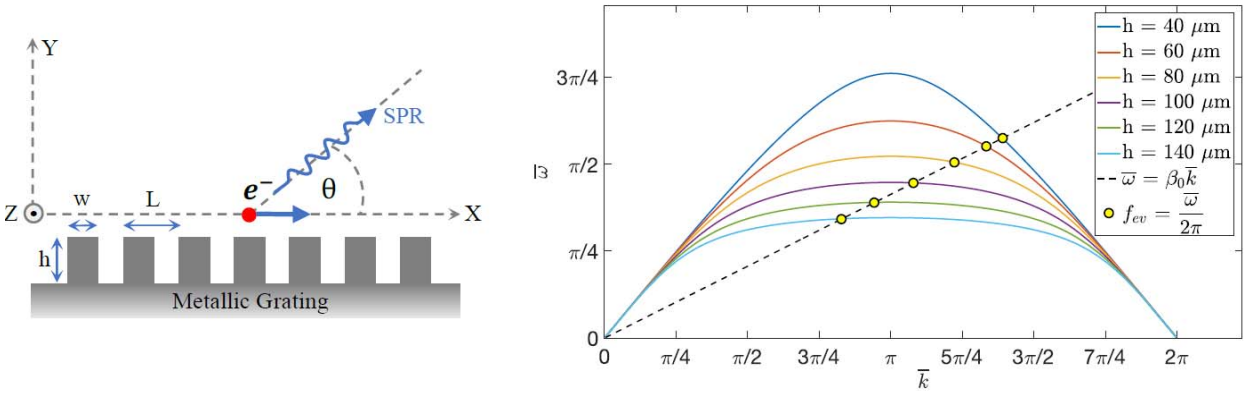

Fig. 30. Smith-Purcell radiation and its dispersion relation (k) for different groove's height h. Here groove's width w is fixed at 60 μm and other parameters are kept as the same as in P. Zhang, L. K. Ang, and A. Gover, Phys. Rev. ST Accel. Beams, 18, 020702 (2015).

3.4 Relativistic quantum electrodynamics plasma physics in supercritical fields

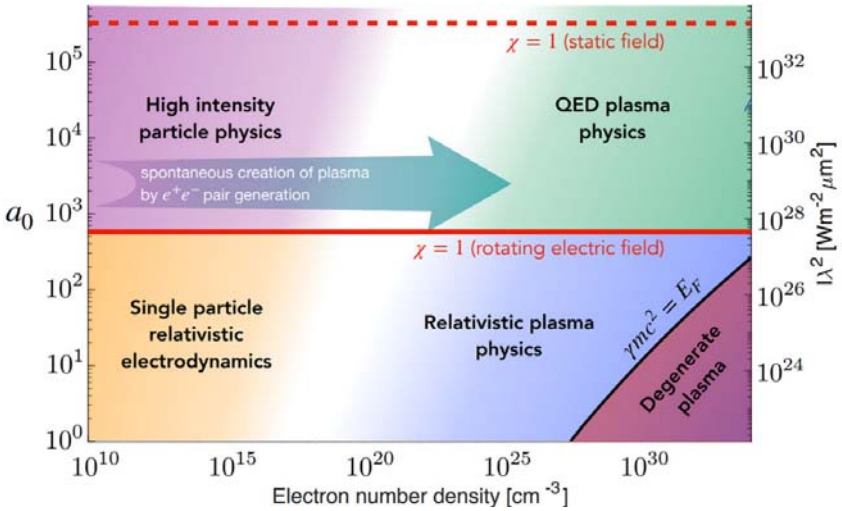

Fig. 31. Different regimes of strong field physics as a function of plasma density and either field strength a_0 (left scale) or laser intensity (right scales). The line $\chi = 1$ in the electron rest frame assumes a rotating configuration with the electron Lorentz factor being $\gamma = a_0$ [26]**.**

In collaboration with University of Michigan, Lawrence Berkeley National Laboratory, University of California at San Diego, we jointly published an invited Perspective article on quantum electrodynamics (QED) plasmas, featured in Physics of Plasmas [26]. Since the invention of chirped pulse amplification, which was recognized by a Nobel Prize in physics in 2018, there has been a continuing increase in available laser intensity. Combined with advances in our understanding of the kinetics of relativistic plasma, studies of laser-plasma interactions are entering a new regime (Fig. 31) where the physics of relativistic plasmas is strongly affected by strong-field QED processes, including hard photon emission and electron–positron pair production. This coupling of quantum emission processes and relativistic collective particle dynamics can result in dramatically new plasma physics phenomena, such as the generation of dense electron-positron pair plasma from near vacuum, complete laser energy absorption by QED processes, or the stopping of an ultrarelativistic electron beam, which could penetrate a cm of lead, by a hair's breadth of laser light. In addition to being of fundamental interest, it is crucial to study this new regime to understand the next generation of ultra-high intensity laser-matter experiments and their resulting applications, such as high energy ion, electron, positron, and photon sources for fundamental physics studies, medical radiotherapy, and next generation radiography for homeland security and industry.

3.5 Gas breakdown and plasma discharge

3.5.1 Effects of surface protrusion in DC microdischarges

Microdischarges have received considerable attention because of their wide industrial applications, such as plasma display panels (PDPs), ion sources, microelectromechanical systems (MEMS), microchips, etc. Due to the greatly reduced discharge dimensions, the size of

microdischarge device is usually limited by the basic plasma characteristic length, such as the sheath length, Debye length and Larmor length. The discharge properties in the micron-scale gaps at high pressure cannot be easily predicted, especially with the presence of the surface roughness and surface protrusion on the electrode. The surface roughness and protrusions might appear on the electrode due to the manufacture deficiency. The surface protrusions on the electrode usually lead to an electric field enhancement, which have profound effects on the gas breakdowns and high-pressure stable microdischarges.

We investigated the electric field enhancement due to the presence of cathode surface protrusion in the atmospheric DC microdischarges, and studied the plasma sheath properties [27], gas breakdown characteristics [28], Paschen's curve [29], and mode transition with electric field non-uniformity [30]. These works are summarized in [31]. We found that the surface protrusion on the cathode electrode results in a combined Paschen's curve, which transits from the long-gap behavior at low pressure to the short-gap behavior at high pressure, resulting in relatively low breakdown voltages in a wider pressure range (Fig. 32).

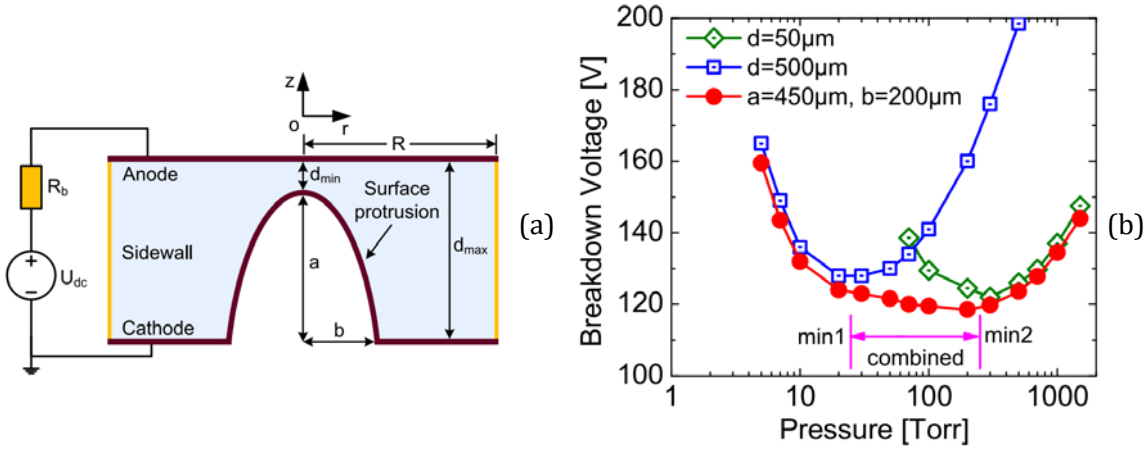

Fig. 32. (a) A microgap with a hemi-ellipsoidal protrusion on the cathode surface filled with Argon, (b) The calculated breakdown voltage as a function of gas pressure for a cathode with hemi-ellipsoidal protrusion (a = 450 μm and b = 200 μm) compared to the parallel-plate gap with d = 50 μm and d = 500 μm, spanning the maximum and minimum gap distance in (a) [29]**.**

The paper [28] on gas breakdown with a protrusion on the electrode is highlighted as a Featured Article in Applied Physics Letters. The related work also resulted in a provisional US patent on controlling microscale gas breakdown via electrode surface engineering [32], filed through the Michigan State University patent office.

3.5.2 Gas breakdown and discharges near microstructures

We studied gas breakdown characteristics in microgaps with multiple concentric protrusions on the cathode (Fig. 33) in the transition from the Townsend to the subnormal glow discharge regime, using a two-dimensional hydrodynamic model [33]. It is found that when the protrusion spacing is small, the shielding effect can play a more important role in the breakdown voltage

rather than the protrusion aspect ratio. Increasing the protrusion spacing decreases the shielding effect, which lowers the breakdown voltage in both low- and high-pressure regimes.

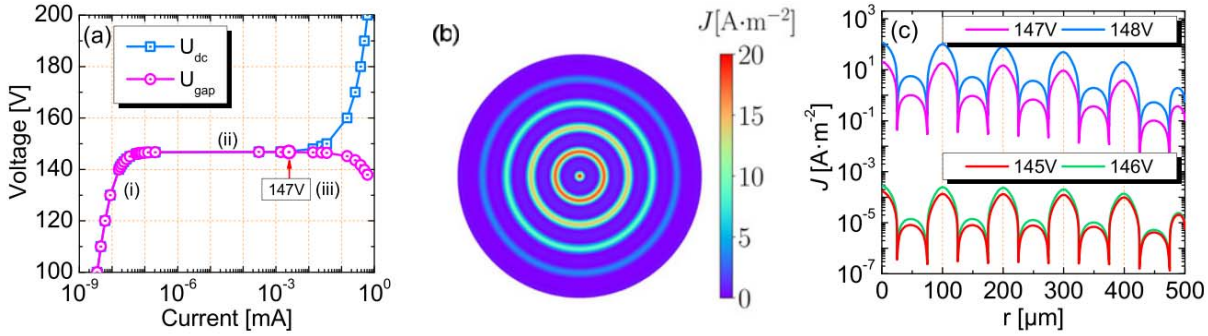

Fig. 33. Gas breakdown characteristics in microgaps with multiple concentric protrusions on the cathode: (a) Voltage-current characteristics with the applied voltage increased from 100 to 200 V; (b) the current density distribution on the cathode with multiple concentric protrusions with applied voltage U_{dc} = 147 V; (c) the radial current density distributions with different U_{dc}. In the calculation, Argon gas pressure p = 500 Torr, protrusion height a = 50 μm, half width b = 25 μm, and protrusion separation X = 100 μm. [33]

We demonstrated the formation and transition behaviors of a microplasma around microstructure arrays at different gas pressures via two-dimensional particle-in-cell/Monte Carlo collision simulations [34]. The collisional and non-collisional components of the electron power absorption are decomposed [35], which were seldomly investigated for microdischarges previously. The results are helpful for understanding the microplasma formation with nonplanar electrodes, which inform the scaling, design, and optimization of microplasma array devices across a wide range of pressure regimes in practical applications.

3.5.3 Plasma discharge similarity and frequency scaling

We also studied the transition characteristics of low-temperature plasma similarity laws from low to high ionization degree regimes [36]. The results are beneficial for utilizing the similarity laws in a wide range of ionization degree regimes, which is essential for correlating plasma characteristics in geometrical similar vessels of various scales.

We reviewed electrical breakdown from macro to micro/nano scales [37]. Fundamental theories of electrical breakdown are revisited with brief explanations. The dominant cathode processes, including secondary emission, field emission, thermionic emission, and their combined effects, are introduced for electrical breakdown under different conditions. The key impact factors of electrical breakdown, such as electrode surface morphology, and breakdown characteristics, such as the modified Paschen's curve, are interpreted with detailed explanations.

We reported the fully kinetic results from particle-in-cell/Monte Carlo collision simulations that unambiguously demonstrate the similarity of radio frequency (rf) discharges in nonlocal regimes where the electron energy relaxation length is much larger than the gap dimension [38]. The

results explicitly validate the scaling laws in nonlocal kinetic regimes, indicating promising application potentials of the similarity transformations across a wide range of kinetic regimes.

We verified the similarity law (SL) and show a violation of frequency scaling (f-scaling) in low-pressure capacitive radio frequency (rf) plasmas via fully kinetic particle-in-cell simulations [39]. We generalized similarity theory based on the scaling and solution invariance of the Boltzmann equation, coupled with the Poisson equation, and demonstrated similarity laws for radio-frequency (rf) discharge plasmas across three nonlinear transitional regimes, namely, the alpha-gamma mode transition, the stochastic-Ohmic-heating mode transition, and the bounce-resonance-heating mode transition [40].

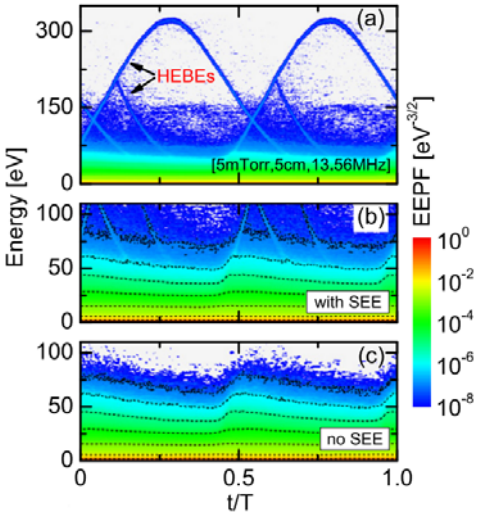

Fig. 34. (a) Temporal electron energy probability function (EEPF) with wavy high-energy tails and bifurcations, indicating the presence of high energy ballistic electrons (HEBEs); (b) zoomed part of the EEPF with SEE; (c) temporal EEPF without SEE while other conditions are maintained [41]**.**

We also demonstrated the presence of a small number of high-energy ballistic electrons (HEBEs) that originate from secondary electrons in low-pressure radio-frequency (rf) plasmas [41]. The kinetic behaviors of the HEBEs are illustrated through electron energy probability functions from the fully kinetic particle-in-cell simulations, showing two wavy high-energy tails and two bifurcations during one rf cycle (Fig. 34). Test-particle simulations and a semi-analytical method associated with nonlocal electron kinetics are performed to characterize the HEBE trajectories, which reveal the ballistic nature of the HEBEs and their typical bouncing features between the rf sheaths.

References (This AFOSR YIP Grant is acknowledged in each journal article or patent below)

[1] Y. Luo and P. Zhang, Ultrafast strong-field photoelectron emission due to two-color laser fields, Phys. Rev. B **98**, 165442 (2018).

[2] Y. Luo and P. Zhang, Analysis of two-color laser-induced electron emission from a biased metal surface using an exact quantum mechanical solution, Phys. Rev. Applied **12**, 044056 (2019).
[3] Y. Luo, J. Luginsland, and P. Zhang, Interference modulation of photoemission from biased metal cathodes driven by two lasers of the same frequency, AIP Advances **10**, 075301 (2020).
[4] Y. Luo, Y. Zhou, and P. Zhang, Few-cycle optical-field-induced photoemission from biased surfaces: An exact quantum theory, Phys. Rev. B **103**, 085410 (2021).
[5] Y. Luo and P. Zhang, Ultrafast optical-field-induced photoelectron emission in a vacuum nanoscale gap: An exact analytical formulation, Appl. Phys. Lett. **119**, 194101 (2021).
[6] X. Xiong, Y. Zhou, Y. Luo, X. Li, M. Bosman, L. K. Ang, P. Zhang, and L. Wu, Plasmon-Enhanced Resonant Photoemission Using Atomically Thick Dielectric Coatings, ACS Nano **14**, 8806 (2020).
[7] P. Zhang, L. Wu, X. Xiong, and Y. Zhou, US Patent Provisional (26 May 2021).
[8] Y. Zhou and P. Zhang, A quantum model for photoemission from metal surfaces and its comparison with the three-step model and Fowler–DuBridge model, Journal of Applied Physics **127**, 164903 (2020).
[9] Y. Zhou and P. Zhang, Quantum efficiency of photoemission from biased metal surfaces with laser wavelengths from UV to NIR, Journal of Applied Physics **130**, 064902 (2021).
[10] P. Zhang, S. B. Fairchild, T. C. Back, and Y. Luo, Field emission from carbon nanotube fibers in varying anode-cathode gap with the consideration of contact resistance, AIP Advances **7**, 125203 (2017).
[11] S. B. Fairchild, P. Zhang, J. Park, T. C. Back, D. Marincel, Z. Huang, and M. Pasquali, Carbon Nanotube Fiber Field Emission Array Cathodes, IEEE Transactions on Plasma Science **47**, 2032 (2019).
[12] S. Banerjee and P. Zhang, A generalized self-consistent model for quantum tunneling current in dissimilar metal-insulator-metal junction, AIP Advances **9**, 085302 (2019).
[13] A. Iqbal, J. Ludwick, S. Fairchild, M. Cahay, D. Gortat, M. Sparkes, W. O'Neill, T. C. Back, and P. Zhang, Empirical modeling and Monte Carlo simulation of secondary electron yield reduction of laser drilled microporous gold surfaces, Journal of Vacuum Science & Technology B **38**, 013801 (2019).
[14] J. Ludwick, A. Iqbal, D. Gortat, J. D. Cook, M. Cahay, P. Zhang, T. C. Back, S. Fairchild, M. Sparkes, and W. O'Neill, Angular dependence of secondary electron yield from microporous gold surfaces, Journal of Vacuum Science & Technology B **38**, 054001 (2020).
[15] Y. Zhou and P. Zhang, Theory of field emission from dielectric coated surfaces, Physical Review Research **2**, 043439 (2020).
[16] P. Zhang, Y. S. Ang, A. L. Garner, A. Valfells, J. W. Luginsland, and L. K. Ang, Space-charge limited current in nanodiodes: Ballistic, Collisional and Dynamical Effects, J. Appl. Phys. **129**, 100902 (2021).
[17] S. Sun, X. Sun, D. Bartles, E. Wozniak, J. Williams, P. Zhang, and C.-Y. Ruan, Direct imaging of plasma waves using ultrafast electron microscopy, Structural Dynamics **7**, 064301 (2020).

[18] S. Banerjee, J. Luginsland, and P. Zhang, A Two Dimensional Tunneling Resistance Transmission Line Model for Nanoscale Parallel Electrical Contacts, Sci Rep **9**, 14484 (2019).
[19] S. Banerjee, P. Wong, and P. Zhang, Contact Resistance and Current Crowding in Tunneling Type Circular Nano-contacts, J. Phys. D: Appl. Phys. (2020).
[20] S. Banerjee, L. Cao, Y. S. Ang, L. K. Ang, and P. Zhang, Reducing Contact Resistance in Two-Dimensional-Material-Based Electrical Contacts by Roughness Engineering, Phys. Rev. Applied **13**, 064021 (2020).
[21] P. Yang, S. Banerjee, W. Kuang, Y. Ding, Q. Ma, and P. Zhang, Current crowding and spreading resistance of electrical contacts with irregular contact edges, J. Phys. D: Appl. Phys. **53**, 485303 (2020).
[22] P. Zhang, S. Banerjee, and J. Luginsland, US Patent No. US10755975B2 (25 August 2020).
[23] S. Banerjee, J. Luginsland, and P. Zhang, Interface Engineering of Electrical Contacts, Phys. Rev. Applied **15**, 064048 (2021).
[24] P. Zhang, J. Park, S. B. Fairchild, N. P. Lockwood, Y. Y. Lau, J. Ferguson, and T. Back, Temperature Comparison of Looped and Vertical Carbon Nanotube Fibers during Field Emission, Applied Sciences **8**, 1175 (2018).
[25] P. Wong, P. Zhang, and J. Luginsland, Recent theory of traveling-wave tubes: a tutorial-review, Plasma Res. Express **2**, 023001 (2020).
[26] P. Zhang, S. S. Bulanov, D. Seipt, A. V. Arefiev, and A. G. R. Thomas, Relativistic plasma physics in supercritical fields, Physics of Plasmas **27**, 050601 (2020).
[27] Y. Fu, P. Zhang, J. P. Verboncoeur, A. J. Christlieb, and X. Wang, Effect of surface protrusion on plasma sheath properties in atmospheric microdischarges, Physics of Plasmas **25**, 013530 (2018).
[28] Y. Fu, P. Zhang, and J. P. Verboncoeur, Gas breakdown in atmospheric pressure microgaps with a surface protrusion on the cathode, Appl. Phys. Lett. **112**, 254102 (2018).
[29] Y. Fu, P. Zhang, and J. P. Verboncoeur, Paschen's curve in microgaps with an electrode surface protrusion, Appl. Phys. Lett. **113**, 054102 (2018).
[30] Y. Fu, J. Krek, P. Zhang, and J. P. Verboncoeur, Evaluating microgap breakdown mode transition with electric field non-uniformity, Plasma Sources Science Technology **27**, 095014 (2018).
[31] Y. Fu, J. Krek, P. Zhang, and J. P. Verboncoeur, Gas Breakdown in Microgaps With a Surface Protrusion On the Electrode, IEEE Transactions on Plasma Science **47**, 2011 (2019).
[32] Y. Fu, P. Zhang, and J. P. Verboncoeur, US Patent provisional number 62/711,109 (26 July 2019).
[33] Y. Fu, P. Zhang, J. Krek, and J. P. Verboncoeur, Gas breakdown and its scaling law in microgaps with multiple concentric cathode protrusions, Appl. Phys. Lett. **114**, 014102 (2019).
[34] Y. Fu, H. Wang, B. Zheng, P. Zhang, Q. H. Fan, X. Wang, and J. P. Verboncoeur, Direct current microplasma formation around microstructure arrays, Appl. Phys. Lett. **118**, 174101 (2021).
[35] Y. Fu, B. Zheng, P. Zhang, Q. H. Fan, and J. P. Verboncoeur, Transition characteristics and electron kinetics in microhollow cathode discharges, Journal of Applied Physics **129**, 023302 (2021).

[36] Y. Fu, J. Krek, D. Wen, P. Zhang, and J. P. Verboncoeur, Transition of low-temperature plasma similarity laws from low to high ionization degree regimes, Plasma Sources Sci. Technol. **28**, 095012 (2019).
[37] Y. Fu, P. Zhang, J. P. Verboncoeur, and X. Wang, Electrical breakdown from macro to micro/nano scales: a tutorial and a review of the state of the art, Plasma Res. Express **2**, 013001 (2020).
[38] Y. Fu, B. Zheng, P. Zhang, Q. H. Fan, J. P. Verboncoeur, and X. Wang, Similarity of capacitive radio-frequency discharges in nonlocal regimes, Physics of Plasmas **27**, 113501 (2020).
[39] Y. Fu, B. Zheng, D.-Q. Wen, P. Zhang, Q. H. Fan, and J. P. Verboncoeur, Similarity law and frequency scaling in low-pressure capacitive radio frequency plasmas, Appl. Phys. Lett. **117**, 204101 (2020).
[40] Y. Fu, H. Wang, B. Zheng, P. Zhang, Q. H. Fan, X. Wang, and J. P. Verboncoeur, Generalizing Similarity Laws for Radio-Frequency Discharge Plasmas across Nonlinear Transition Regimes, Phys. Rev. Applied **16**, 054016 (2021).
[41] Y. Fu, B. Zheng, D.-Q. Wen, P. Zhang, Q. H. Fan, and J. P. Verboncoeur, High-energy ballistic electrons in low-pressure radio-frequency plasmas, Plasma Sources Sci. Technol. **29**, 09LT01 (2020).

4.0 External Collaborations

The PI has extensive collaborations with colleagues at

(a) DoD and DoE labs: Air Force Research Laboratory (AFRL) at Kirtland and at Wright-Patterson, and Lawrence Berkeley National Laboratory.

(b) universities: University of Michigan, University of Cincinnati, University of Cambridge, Purdue University, Singapore University of Technology and Design, Reykjavik University (Iceland), UC San Diego, Rice University, University of Southern California, University of Huddersfield (UK), and Xi'an Jiaotong University (China).

(c) industries: Confluent Sciences, Lam Research.

The archival journal publications and patents (issued and pending) resulting from these collaborations are listed below, by institutions.

<u>Air Force Research Laboratory</u>

With Dr. N. P. Lockwood at AFRL-Kirtland [24]; and with Drs. Steven Fairchild and T. C. Beck at AFRL-Wright-Patterson [10, 11, 13, 14, 24].

With Drs. Brad Hoff and Wilkin Tang at AFRL-Kirtland, the PI (P. Zhang) served as Guest Editor for the 2020 High Power Microwave (HPM) Special Issue in IEEE Transaction on Plasma Science (IEEE TPS).

Lawrence Berkeley National Laboratory

With Dr. S. S. Bulanov [26].

University of Michigan

With Professor Y. Y. Lau [24]

With Professor A. G. R. Thomas [26]

University of Cincinnati

With Professor M. Cahay [13, 14].

University of Cambridge

With Professors D. Gortat, M. Sparkes and W. O'Neill [13, 14]

Singapore University of Technology and Design

With Professor L. K. Ang [6, 16, 20]

With Professor L. Wu [6, 7]

With Professor Y. S. Ang [16, 20]

Reykjavik University (Iceland)

With Professor A. Valfells [16]

Purdue University

With Professor A. Garner [16]

UC San Diego

With Professor A. V. Arefiev [26]

Rice University

With Professor M. Pasquali [11]

University of Huddersfield (UK)

With Professor R. Seviour, the PI (P. Zhang) served as Guest Editor for the 2020 High Power Microwave (HPM) Special Issue in IEEE Transaction on Plasma Science (IEEE TPS).

Xi'an Jiaotong University (China)

With Professor W. Kuang [21]

Confluent Sciences

With Dr. John Luginsland [3, 16, 18, 22, 23, 25]

Lam Research

With Drs. Y. Ding and Q. Ma [21]

5.0 Personnel

Faculty

Professor Peng Zhang, PI.

Research staff participation

Patrick Wong, Postdoctoral Researcher

Yangyang Fu, Postdoctoral Researcher

Deqi Wen, Postdoctoral Researcher

Asif Iqbal, Postdoctoral Researcher

Graduate student supported by this Grant

(Dr.) Yi Luo, (Dr.) Sneha Banerjee, Yang Zhou (partial)

Graduate students participation

(Dr.) Asif Iqbal, Zizhuo Huang, (Dr.) Janez Krek, Md Arifuzzaman Faisal, Ayush Paudel

Undergraduate Student Participation

Penglu Yang, Michael Dittman, Zizhuo Huang, Aryan Verma

6.0 Publications (which acknowledged this grant)

Archival refereed journals: 38 published, 3 under review. [List given at the end of Section 3.5.3]

PhD theses:

Yi Luo, "Theoretical modeling of ultrafast optical-field induced photoelectron emission from biased metal surfaces", PhD Thesis, Michigan State University, 2021.

Sneha Banerjee, "Modeling of nanoscale electrical junctions and electrical contacts", PhD Thesis, Michigan State University, 2021.

Issued and Pending Patents:

1. P. Zhang, S. Banerjee, J. Luginsland, "Tunneling Electrical Contacts", US Patent Provisional Number 62/688,515; converted to nonprovisional United States application 16/448,160 on 6/21/2019; Pub. No.: US 2019/0393087 A1, Pub. Date: Dec. 26, 2019; Patent 11 No.: US 10,755,975 B2, Date of Patent: Aug. 25, 2020.
2. Y. Fu, P. Zhang, J. Verboncoeur, "Microscale gas breakdown device and process", US Patent provisional number 62/711,109; converted to nonprovisional United States application 16/523,255 on 7/26/2019; Pub. No.: US 2020/0033293 A1, Pub. Date: Jan. 30, 2020.
3. P. Zhang, L. Wu, X. Xiong, and Y. Zhou, "Thin Dielectric Coated Plasmonic Photoemitter", US Patent Provisional filed on 5/26/2021.

Conference Abstracts: > 50 (IVEC, ICOPS, IVNC, GEC, Asia-Pacific Conference on Plasma and Terahertz Science (APCOPTS), Photocathode Physics for Photoinjectors (P3) Workshop, European Advanced Energy Materials Congress)

Major Invited talks:

1. P. Zhang, "Recent development on the modeling of laser induced electron emission", Photocathode Physics for Photoinjectors (P3) Workshop, October 15-17, 2018, Santa Fe, New Mexico, USA.

2. P. Zhang, "Recent Development on the Modeling of Laser Induced Electron Emission", The 2018 Asia-Pacific Conference on Plasma and Terahertz Science (APCOPTS), August 15-18, Xi'an, China.

3. P. Zhang, "Modeling of Ultrafast and Nanoscale Interfacial Charge Transport", European Advanced Energy Materials Congress 2018, March 25 – 28, 2018, Stockholm, Sweden.

4. P. Zhang, "Ultrafast and Nanoscale Electron Emission and Transport", Center for Ultrafast Optical Science (CUOS) Seminar, the University of Michigan, Ann Arbor, MI, 02/02/2018.

5. P. Zhang, “Recent advances on the modeling of electron transport at ultrashort spatiotemporal scales”, IEEE Nuclear & Plasma Sciences Society Singapore Chapter Seminar, Singapore, 5/7/2019.

6. P. Zhang, Y. Luo, and Y. Zhou, “A general quantum model for thermionic-field-photoelectron emission”, PIC-NIC Virtual Workshop, October 20 - 21, 2020, Sandia National Laboratories, Albuquerque, NM, USA.

7. P. Zhang, “Electron Emission and Plasma Interaction with Intense Fields”, Department of Nuclear Engineering and Radiological Sciences, University of Michigan, Ann Arbor, MI, 01/22/2020.

8. P. Zhang, “Modeling of Nanoscale Electrical Junctions and Electrical Contacts”, 2nd Edition Nanotechnology and Nanomaterials Virtual (V-Nano2021), 16-17 July 2021.

9. P. Zhang, Y. Luo, Y. Zhou, “Exact Analytical Solution for Pulsed Laser Induced Photoemission from Biased Surfaces”, The 48th IEEE International Conference on Plasma Science (ICOPS), Sep 12-16, 2021, Virtual, USA.

10. P. Zhang, “Exact Quantum Solution for Photoemission at Ultrafast and Ultra small Scales”, Photocathode Physics for Photoinjectors Workshop (P3 2021), Nov 10-12, 2021, SLAC, Virtual, USA.

7.0 Awards and Honors (during the performance period of this YIP grant)

a. Peng Zhang, PI, 2020 IEEE Nuclear & Plasma Sciences Society (NPSS) Early Achievement Award.

b. Peng Zhang, PI, 2020 Young Investigator Program (YIP) Award, Office of Naval Research (2020).

c. Yi Luo, PhD student, 2018 Michigan Institute for Plasma Science and Engineering (MIPSE) Graduate Student Symposium Best Presentation Award.

d. Asif Iqbal, PhD student, 2019-2020 MIPSE Graduate Student Fellowship.

e. Asif Iqbal, PhD student, 2019 MIPSE Graduate Student Symposium Best Presentation Award.

f. Asif Iqbal, PhD student, 2019-2020 MSU Electrical Engineering Outstanding Graduate Student Award.

g. Sneha Banerjee, PhD student, 2020 MIPSE Graduate Student Symposium Best Presentation Award.

h. Sneha Banerjee, PhD student, 2020-2021 MSU Graduate School Writing Fellow.

i. Sneha Banerjee, PhD student, 2020-2021 MIPSE Graduate Student Fellowship.

j. Sneha Banerjee, PhD student, second place in 2021 Michigan State University Three Minute Thesis (3MT) competition.

k. Asif Iqbal, PhD student, 2021 MIPSE Graduate Student Symposium Best Presentation Award.

l. Yi Luo, PhD student, 2021-2022 MIPSE Fellowship [declined].

m. Sneha Banerjee, PhD student, 2021 IEEE Nuclear and Plasma Sciences Society (NPSS) Graduate Scholarship Award.

n. Sneha Banerjee, PhD student, 2020 – 2021 MSU Electrical Engineering Outstanding Graduate Student Award.